On the dynamics of a shock–bubble interaction

By JAMES J. QUIRK[1]† AND S. KARNI[2]‡

[1]Institute for Computer Applications in Science and Engineering, NASA Langley Research Center, Hampton, VA 23681, USA

[2]Courant Institute of Mathematical Sciences, New York University, 251 Mercer St., New York, NY 10012, USA

We present a detailed numerical study of the interaction of a weak shock wave with an isolated cylindrical gas inhomogeneity. Such interactions have been studied experimentally in an attempt to elucidate the mechanisms whereby shock waves propagating through random media enhance mixing. Our study concentrates on the early phases of the interaction process which are dominated by repeated refractions and reflections of acoustic fronts at the bubble interface. Specifically, we have reproduced two of the experiments performed by Haas & Sturtevant: a Mach 1.22 planar shock wave, moving through air, impinges on a cylindrical bubble which contains either helium or Refrigerant 22. These flows are modelled using the two-dimensional compressible Euler equations for a two-component fluid (air–helium or air–Refrigerant 22). Utilizing a novel shock-capturing scheme in conjunction with a sophisticated mesh refinement algorithm, we have been able to reproduce numerically the intricate mechanisms that were observed experimentally, e.g. transition from regular to irregular refraction, cusp formation and shock wave focusing, multi-shock and Mach shock structures, and jet formation. The level of agreement lends credibility to a number of observations that can be made using information from the simulations for which there is no experimental counterpart. Thus we can now present an updated description for the dynamics of a shock–bubble interaction which goes beyond that provided by the original experiments.

1. Introduction

In an extremely lucid paper, Haas & Sturtevant (1987) presented an experimental study of the interaction of weak shock waves with isolated inhomogeneities that took the form of either spherical or cylindrical bubbles. They argued that idealized experiments were necessary to shed light on the complex phenomenological behaviour whereby shock waves propagating through random media can alter the structure of fluid inhomogeneities. To this end, their experiments were a resounding success. A number of shadowgraphs were produced which provide important insight into mechanisms such as transition from regular to irregular refraction, folding processes, shock wave focusing, distortion of the bubble interface and vortex formation. However, given the nature of the experiments, certain subtleties of the interaction process were inevitably left unexplained. Recall that such experiments are extremely difficult to

† Present address: Graduate Aeronautical Laboratories, California Institute of Technology, Pasadena CA 91125, USA.

‡ On leave from Temple University, Philadelphia, PA 19122, USA.

control since they are conducted under imperfect conditions. For example, diffusion occurs across the membrane that forms the bubble interface and so the precise properties of the gas inhomogeneity are not known (Abd-El-Fattah & Henderson 1978a,b). Moreover, when the shock impinges on the bubble the membrane does not always rupture cleanly and can interfere with the flow (Rupert 1992), as does the support structure needed to hold the bubble in place. There are also difficulties with the repeatability of the experiment due to variations in the incident shock strength (Haas & Sturtevant 1987), and problems with the interpretation of the flow visualization images due to unwanted three-dimensional effects (Wang & Widhopf 1990). Other problems arise in that certain quantities of interest cannot be measured directly, either because of their intrinsic nature (e.g. vorticity) or because of practical limitations in the experimental set-up.

Given this background, the present work is an attempt to clarify the physical mechanisms observed by Haas & Sturtevant (1987) using high-resolution numerical simulations to provide key information missing from previous analyses. For example, although Haas & Sturtevant were able to use the theory of geometrical acoustics to gain a good understanding of their experimental observations, this theory ignores wave nonlinearities and so fails to account for all flow features. Similarly, while von Neumann theory (1963) is exact, within its assumptions, it cannot cope with regions of non-uniform flow and therefore is not strictly applicable to shock interactions at curved interfaces (Ben-Dor & Takayama 1985). On the other hand, Whitham's theory (1957, 1958) and its extensions (Catherasoo & Sturtevant 1983; Schwendeman 1988) can cope with curved interfaces, but the theory does not take proper account of reflected waves and cannot provide any details for the flow structure behind the incident and refracted shock fronts. Hence the need for numerical simulations – simulations provide a controlled means of isolating genuine flow phenomenology from experimental artifact and can provide global details of the flow dynamics to supplement the idealized, local descriptions provided by theory. For the case of shock refraction at a planar interface, Henderson, Colella & Puckett (1991) have demonstrated that careful simulations can be used to improve the classification of reflection-refraction phenomena which arose from experiment and analysis (Abd-El-Fattah & Henderson 1978a,b). Here we aim to shed more light on the refraction process at a curved interface.

Several numerical studies have already been inspired by the experiments of Haas & Sturtevant (1987): Picone & Boris (1988) and Yang, Kubota & Zukoski (1993, 1994) performed computations aimed at determining the long-time evolution of the bubble inhomogeneities; Löhner, Picone & Boris (1988) investigated the early-time dynamics of the interaction process; Samtaney & Zabusky (1994) performed simulations to validate a prediction model for the circulation produced by the interactions. Apart from this last reference, these earlier studies employed a single-gas flow model and so did not represent closely the binary systems used in the experiment. More specifically, since some desired density jump must be imposed across the bubble interface, with a single-gas model the bubble cannot be in thermal equilibrium with its surroundings, as was the case with the experiments. Consequently the error in temperature will be arbitrarily large, dependent on the required density ratio (for a helium bubble in air the temperature would be 2.08 times too high). Admittedly, for the cases studied here the errors so introduced are not catastrophic and to some extent may be tolerated. However, one motivation for studying a shock–bubble interaction is to investigate mechanisms whereby air and fuel can be mixed in the short transit time open to a supersonic combustion system (Marble, Hendricks & Zukoski 1987), an application

where gross errors in the temperature field could not be tolerated. In addition to the shortcoming of the flow model, all the referenced studies are under-resolved and therefore prone to misinterpretation.

Our computational approach is shaped by a desire to avoid these shortcomings. First, account is taken of the different gas components (air and helium or air and Refrigerant 22 depending upon the experiment being simulated). Although this represents but a small modelling generalization, numerical difficulties are introduced that have led us to adopt a novel shock-capturing scheme (Karni 1994). Second, we utilize a sophisticated adaptive mesh refinement algorithm (Quirk 1991) that can reduce by several hundred-fold the cost of performing detailed simulations and so allows for simulations that would otherwise be prohibitively expensive.

The organization for the rest of this paper is as follows. In the next section we present our flow model and describe the motivation behind our choice of integration scheme. In §3 we describe the major components of our numerical method, then in §4 we detail the computational set-up for the experiments that we have simulated. This is followed by four sections of results and discussion. First, in §5 we present a qualitative comparison with experiment, concentrating on flow visualization. Then we present two quantitative comparisons with experiment: one section deals with the velocities of certain key flow features, the other deals with the measurement of pressure traces at various locations along the axis of flow symmetry. These comparisons are followed by a discussion on the production of vorticity resulting from the passage of the shock through the bubble inhomogeneity. Although this discussion goes beyond the main purpose of this paper it is pertinent to several recent studies aimed at determining the long-time evolution of the bubble. Finally, in §9 we summarize the main results of our study.

2. Flow model

As Picone & Boris (1988) observed, diffusive effects do not play a major role in the early dynamics of the present shock–bubble interactions, because the timescales are too short. They estimated the kinematic viscosity to be 0.2 cm^2 s^{-1} which translates to an effective viscous lengthscale of 0.089 mm at the end of a 400 μs interaction, i.e. 1/1000 of the height of the duct used in the experiments. Therefore a direct numerical simulation would have to employ a mesh spacing at least an order of magnitude smaller than this lengthscale, to stand any chance of resolving the viscous structures accurately, and so would prove inordinately expensive compared to an inviscid simulation. In view of this, we took the two-component compressible Euler equations as the basis for our investigation.

In a Cartesian space (x, y), these equations may be cast in conservation form using the variables $W = (\rho, \rho u, \rho v, E, \rho Y)^t$:

$$W_t + F(W)_x + G(W)_y = 0;$$

$$F(W) = \begin{pmatrix} \rho u \\ \rho u^2 + p \\ \rho uv \\ u(E + p) \\ \rho u Y \end{pmatrix}; \quad G(W) = \begin{pmatrix} \rho v \\ \rho vu \\ \rho v^2 + p \\ v(E + p) \\ \rho v Y \end{pmatrix}. \quad (2.1)$$

The equations are written for a mixture of two fluids; ρ is the density of a binary mixture whose mass fractions are Y for component one and $1 - Y$ for component two. Thus it is assumed that the fluid components are in pressure equilibrium and
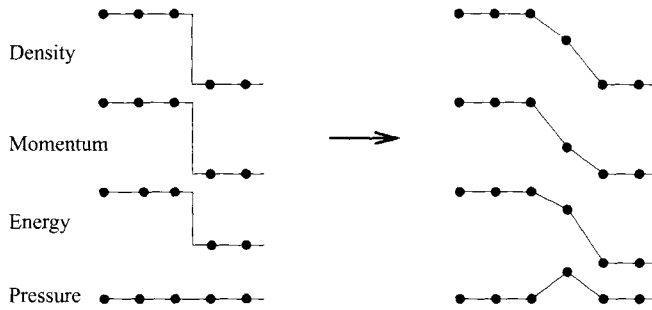
FIGURE 1. Pressure fluctuation at a material interface due to numerical smearing.

move with a single velocity whose components are u and v in the x- and y-directions, respectively. This assumption of no velocity slip is reasonable only if the density variation between components is moderate as is generally the case with two gases. Both fluid components are taken to be perfect gases, with ratios of specific heat $\gamma_1 = Cp_1/Cv_1$ and $\gamma_2 = Cp_2/Cv_2$. Therefore, the pressure, p, is given by

$$p = (\gamma(Y) - 1)(E - \tfrac{1}{2}\rho u^2 - \tfrac{1}{2}\rho v^2) \tag{2.2}$$

where E is the total energy of the mixture per unit volume, and $\gamma(Y)$ is the effective ratio of specific heats dependent on the species concentration, Y, and is found from standard thermodynamic reasoning to be

$$\gamma(Y) = \frac{\gamma_1 Cv_1 Y + \gamma_2 Cv_2(1 - Y)}{Cv_1 Y + Cv_2(1 - Y)}. \tag{2.3}$$

It is well known that solutions to (2.1) may develop discontinuous shock fronts, across which the governing equations are no longer valid in their differential form, and that using Gauss's divergence theorem (2.1) may be recast into an integral form which remains valid at a shock:

$$\frac{\partial}{\partial t} \int\int_D W \mathrm{d}x \mathrm{d}y + \oint_{\partial D} F \mathrm{d}y - G \mathrm{d}x = 0. \tag{2.4}$$

Equation (2.4) is the basis for so-called conservative shock-capturing schemes: discretizations in which numerical approximations to the flux vectors F and G are used to evolve the field solution, W. Irrespective of the flux formulation, however, a shock-capturing scheme results in a smeared 'viscous' shock profile rather than the perfect discontinuity admitted by the governing equations (unless the discontinuity coincides with a cell interface). Although artificially smeared, a shock captured by a conservative discretization can be shown to have both the correct strength and speed; conversely, a non-conservative discretization may give physically inconsistent solutions (Lax 1954,1972; Hou & Le Floch 1994).

Given this fundamental property, a conservative formulation is almost universally accepted as the starting point for devising a shock-capturing scheme, and to date many successful schemes have been so developed for single-component flows. However, a major concern in extending conservative schemes to multi-component flows is to ensure that fluid components maintain pressure equilibrium across numerically diffused material interfaces (Abgrall 1988; Larrouturou 1991; Ton et al. 1991, Karni 1994a, and Bell et al. 1994). This numerical difficulty is illustrated in figure 1. Even when each of the conserved variables, W, remains monotone as a material interface smears, there is no guarantee that a derived quantity will also remain monotone and
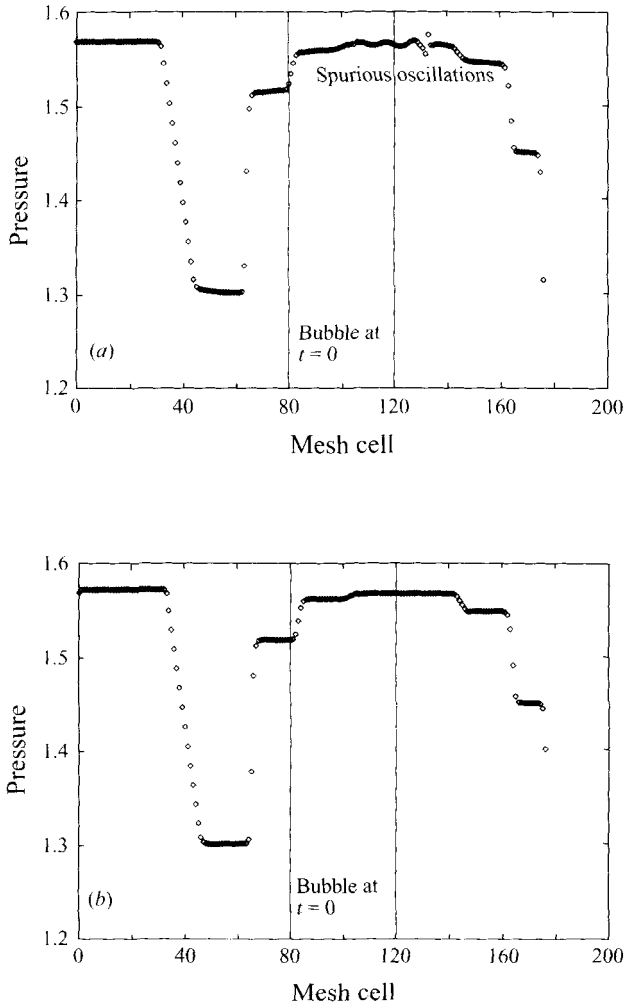
FIGURE 2. Pressure profiles for a one-dimensional 'shock–bubble' interaction obtained using: (*a*) a conservative scheme (Roe 1982); (*b*) the present non-conservative scheme (Karni 1994).

so the pressure that corresponds to the artificial intermediate state can differ from the equilibrium pressure.

Once generated, such pressure fluctuations can propagate and contaminate the solution field. For example, figure 2(*a*) shows a snapshot from a one-dimensional conservative computation of a shock–bubble interaction where the start data are identical to the air–helium case given in §4. Here the initial position of the bubble is marked by the vertical lines and the computed pressure field is shown some time after the shock has passed through the bubble and several reflections and refractions have taken place. Spurious pressure oscillations are clearly visible. For other sets of reasonable data, such oscillations can get even larger. Now since material interfaces can be physically unstable, even slight numerical perturbations can trigger completely incorrect interfacial behaviour (Karni 1995) and are therefore to be avoided. Moreover in a reactive system such pressure perturbations could significantly alter the local release of energy and become amplified.

Numerical problems such as the above can be avoided, if fronts are fitted or

tracked as perfect discontinuities, rather than captured as smeared discontinuities. For example, the multi-fluid tracking algorithm of Colella, Glaz & Ferguson (1989) (also described in Puckett & Saltzman 1992) has been successfully applied to the study of shock refraction at a planar interface (Henderson *et al.* 1991). This algorithm is based on a volume-of-fluid approach and reconstructs material interfaces at the sub-grid level, using the partial volumes of the separate fluid components, so as to obtain appropriate local thermodynamic properties with which to evolve the flow, maintaining pressure equilibrium between components. Closer to the present study, Grove & Menikoff (1990) have successfully employed a front tracking algorithm (Glimm & McBryan 1985) to the interaction of a shock with an air bubble in water. Although effective, both fitting and tracking methods can be awkward to implement in multi-dimensions owing to the logistics of having to deal explicitly with arbitrary shaped interfaces and the topological possibilities this entails.

We prefer to remain within the framework afforded by a shock-capturing philosophy and have adopted an unconventional approach which ensures pressure equilibrium among fluid components in a more straightforward manner. In our approach the Euler system (2.1) is recast using primitive variables, $U = (\rho, u, v, p, Y)^t$, to give

$$U_t + A^p(U)U_x + B^p(U)U_y = 0,$$

$$A^p(U) = \begin{pmatrix} u & \rho & 0 & 0 & 0 \\ 0 & u & 0 & \rho^{-1} & 0 \\ 0 & 0 & u & 0 & 0 \\ 0 & \gamma p & 0 & u & 0 \\ 0 & 0 & 0 & 0 & u \end{pmatrix}; \quad B^p(U) = \begin{pmatrix} v & 0 & \rho & 0 & 0 \\ 0 & v & 0 & 0 & 0 \\ 0 & 0 & v & \rho^{-1} & 0 \\ 0 & 0 & \gamma p & v & 0 \\ 0 & 0 & 0 & 0 & v \end{pmatrix}. \tag{2.5}$$

To see the advantages of this formulation, consider a planar material interface aligned in the x-direction with data such that $\partial/\partial y \equiv 0$. Across the interface, both the pressure, p, and the normal velocity component, u, are constant. It follows that locally the system (2.5) reduces to three completely decoupled *linear* advection equations in ρ, v and Y and that both p and u remain constant. Thus, near the material interface, any consistent discretization of (2.5) will produce oscillation-free solutions without introducing conservation errors.

Conservation errors, however, will occur near shocks and unless some measure is taken to control them, a primitive-variable formulation will prove inadequate. Building on an idea first proposed by Zwas & Roseman (1973), Karni (1992) has developed a set of high-order correction terms which can be used to remove leading-order conservation errors to produce a nearly conservative primitive-variable scheme. This scheme rests on two observations:

(i) numerically captured shocks have 'viscous' profiles which are determined by the truncation error of the discretization scheme;

(ii) a conservative discretization produces a consistent 'viscous' shock profile in the sense that a captured shock has both the correct strength and speed.

In essence, the present primitive-variable scheme employs correction terms to mimic the 'viscous' shock profile of a conservative scheme. In the next section, we outline the derivation of this scheme. But first, we demonstrate that for the above one-dimensional problem it produces oscillation free solutions: cf. figures 2(*a*) and 2(*b*).

3. Numerical method

We now describe the major components of our numerical method. These are: (i) the primitive variable discretization – this provides a sound basis for the integration

of multicomponent flows; (ii) the parallel, adaptive mesh refinement implementation – this is essential to resolve intricate flow features, while maintaining low computational costs; (iii) graphical flow visualization – this facilitates the process of elucidating the phenomena under investigation.

We describe these components in some depth, since many of the details are not available elsewhere, and the components are sufficiently general purpose that they could be used profitably to study phenomena quite unrelated to that studied here.

3.1. *A non-conservative shock-capturing scheme*

Following Strang (1968), we employ dimensional splitting to integrate the system (2.5) with the refinement that correction terms are applied to the right-hand side of each split equation so as to control conservation errors. Thus, we alternate between integrating

$$\boldsymbol{U}_t + \boldsymbol{A}^p(U)\boldsymbol{U}_x = \frac{\Delta t}{2}\boldsymbol{D}_x \qquad \text{and} \qquad \boldsymbol{U}_t + \boldsymbol{B}^p(U)\boldsymbol{U}_y = \frac{\Delta t}{2}\boldsymbol{D}_y. \tag{3.1}$$

The precise form of the correction terms, $\boldsymbol{D}_x$ and $\boldsymbol{D}_y$, depends upon the discretization for the left-hand side of each split equation. Here we derive the correction terms, $\boldsymbol{D}_x$, assuming that the left-hand side of the x-sweep operator has been discretized using Roe's first-order upwind scheme (Roe 1982). In essence, this is done by comparing the x-sweep discretization for the primitive system (2.5) with the analogous x-sweep discretization for the conservative system (2.1).

If Roe's scheme (Roe 1982) is used to solve (2.1), the scheme is a first-order approximation to (2.1) but it is a second-order approximation to the equivalent equation

$$\boldsymbol{W}_t + \boldsymbol{F}(\boldsymbol{W})_x = \boldsymbol{W}_t + \boldsymbol{A}^c(\boldsymbol{W})\boldsymbol{W}_x = \frac{\Delta t}{2}\left(\frac{(|\boldsymbol{A}^c|\boldsymbol{W}_x)_x}{\lambda} - \boldsymbol{W}_{tt}\right) \tag{3.2}$$

where $\lambda = \Delta t/\Delta x$ is the ratio of the time step and mesh size used for the integration and $\boldsymbol{A}^c$ is the Jacobian matrix $\partial\boldsymbol{F}(\boldsymbol{W})/\partial\boldsymbol{W}$. The right-hand side of (3.2) constitutes the leading order terms in the truncation error of the scheme. To leading order, these dissipative terms determine the viscous path across the numerical shock transition. In this case, the numerical viscous path is physically consistent since it is produced by a conservative scheme and so it produces correct shock speeds and jumps.

Similarly, if Roe's upwind scheme is applied to solve equation (2.5), the scheme is a second-order approximation to the equivalent equation

$$\boldsymbol{U}_t + \boldsymbol{A}^p(U)\boldsymbol{U}_x = \frac{\Delta t}{2}\left(\frac{(|\boldsymbol{A}^p|\boldsymbol{U}_x)_x}{\lambda} - \boldsymbol{U}_{tt}\right). \tag{3.3}$$

In general, the two viscous forms (3.2) and (3.3) are different. The former, arising from a conservative discretization, yields shocks that satisfy the Rankine–Hugoniot conditions the latter does not. To enforce consistent shock profiles on the primitive solution, the difference between the two viscous expressions (appropriately transformed) has to be added to the right-hand side of the x-sweep operator for the primitive system to give (3.1) where

$$\boldsymbol{D}_x = \left\{\boldsymbol{T}\left(\frac{(|\boldsymbol{A}^c|\boldsymbol{W}_x)_x}{\lambda} - \boldsymbol{W}_{tt}\right) - \left(\frac{(|\boldsymbol{A}^p|\boldsymbol{U}_x)_x}{\lambda} - \boldsymbol{U}_{tt}\right)\right\} \tag{3.4}$$

and $\boldsymbol{T}$ is the conservative to primitive transformation matrix $\partial\boldsymbol{U}/\partial\boldsymbol{W}$.

If (3.1) is solved by Roe's upwind scheme, with its right-hand side (3.4) appropriately discretized, the solution procedure is conservative to the order of the numerical

approximation. The correction terms may be written entirely in terms of the primitive variables

$$\boldsymbol{D}_x = \frac{\boldsymbol{T}(\boldsymbol{T}^{-1})_x |\boldsymbol{A}^p| \boldsymbol{U}_x}{\lambda} - \boldsymbol{T}(\boldsymbol{T}^{-1})_t \boldsymbol{U}_t. \tag{3.5}$$

Straightforward algebra shows that for the extended Euler system (2.5), the correction terms are given by

$$\boldsymbol{D}_x = \begin{pmatrix} 0 \\ \dfrac{1}{2\rho} \left(\dfrac{c_1 \rho_x u_x + (1/a^2)c_2 u_x p_x + c_4 \left((\rho/a)u_x^2 + (1/\rho a)p_x \rho_x\right)}{\lambda_x} - 4\rho_t u_t \right) \\ \dfrac{1}{2\rho} \left(\dfrac{(1/a^2)c_2 p_x v_x + 4|u|\rho_x v_x + c_4(\rho/a)u_x v_x}{\lambda_x} - 4\rho_t v_t \right) \\ \dfrac{\gamma-1}{2} \left(\dfrac{c_3 \rho u_x^2 + (1/a)c_4 p_x u_x + 2|u|\rho v_x^2}{\lambda_x} - 2\rho \left(u_t^2 + v_t^2\right) \right) \\ 0 \end{pmatrix} \tag{3.6}$$

where

$$c_1 = |u-a| + 2|u| + |u+a|, \qquad c_3 = |u-a| + |u+a|,$$
$$c_2 = |u-a| - 2|u| + |u+a|, \qquad c_4 = |u-a| - |u+a|$$

and a is the sound speed.

The following observations can be made.

(i) If (2.5) is used to replace time derivatives by space derivatives, all terms within $\boldsymbol{D}_x$ are scaled by either one or both of u_x and p_x, hence $\boldsymbol{D}_x$ vanishes near contact surfaces. Consequently, the correction terms, although derived for first-order upwinding, may also be used for second-order upwinding without degrading the latter's superior resolution of contact surfaces (Karni 1992, 1994). Besides, such schemes often reduce to first-order accuracy near shocks anyway, which is precisely where the correction terms come into play.

(ii) The correction terms are derived using asymptotic arguments based on the scheme truncation error. Conservation errors, while significantly reduced, are inherent to the method (Hou & Le Floch 1994; Karni 1992) and are not completely eliminated.

(iii) The correction terms depend on the ratio $\lambda = \Delta t / \Delta x$, and so some variation in their effect is to be expected with changes in Courant number (wave speed*λ). It is our experience that the correction terms work best at Courant numbers close to one, which is the upper bound on the size of time step for the integration process to be stable.

The correction terms for the y-sweep operator (3.1) may be similarly derived and are given by

$$\boldsymbol{D}_y = \begin{pmatrix} 0 \\ \dfrac{1}{2\rho} \left(\dfrac{(1/a^2)c_2 p_y u_y + 4|v|\rho_y u_y + c_4(\rho/a)u_y v_y}{\lambda_y} - 4\rho_t u_t \right) \\ \dfrac{1}{2\rho} \left(\dfrac{c_1 \rho_y v_y + (1/a^2)c_2 v_y p_y + c_4 \left((\rho/a)v_y^2 + (1/\rho a)p_y \rho_y\right)}{\lambda_y} - 4\rho_t v_t \right) \\ \dfrac{\gamma-1}{2} \left(\dfrac{c_3 \rho v_y^2 + (1/a)c_4 p_y v_y + 2|v|\rho u_y^2}{\lambda_y} - 2\rho \left(u_t^2 + v_t^2\right) \right) \\ 0 \end{pmatrix} \tag{3.7}$$

where the coefficients c_1–c_4 are the same as those in (3.6) but with u replaced by v.

Given the derivation of the correction terms, our basic method of flow integration is as follows. The left-hand side of each split equation (3.1) is discretized using a second-order Roe scheme cast in 'fluctuation-and-signal' form (Roe 1982). For the correction terms, temporal derivatives are replaced by spatial derivatives which are then centrally differenced, and pointwise values take the cell-centred values used by Roe's scheme. The correction terms contribute to cell updates via a forward Euler time integration. Thus the x-sweep operator of our nearly conservative primitive-variable scheme takes the form

$$U_i^{n+1} = \mathscr{L}_x^{Roe}(U_i^n) + \Delta t \left[\frac{\Delta t}{2} D_x(U_i^n) \right]$$

where $\mathscr{L}_x^{Roe}$ is the standard Roe evolution operator. The y-sweep operator follows by analogy, and the two operators are alternated so as to arrive at a two-dimensional scheme (Strang 1968).

3.2. *The AMR algorithm – an overview*

The Adaptive Mesh Refinement (AMR) algorithm is a general purpose scheme for integrating systems of hyperbolic partial differential equations. It attempts to reduce the costs of integration by matching the local resolution of the computational grid to the local requirements of the solution being sought. For example, in simulations of gasdynamic flows, a fine mesh is generally used only in the vicinity of shock waves and other flow discontinuities, elsewhere a relatively coarse mesh is employed. Although the computational savings which accrue from local mesh refinement are totally problem dependent, they are often significant; savings of more than five hundred-fold have been obtained for simulations of detonation phenomena (Quirk 1996). The foundations of the AMR algorithm lie in the works of Berger & Oliger (1984) and Berger & Colella (1989), but the derivative outlined here is due to Quirk (1991, 1996).

The AMR algorithm employs a hierarchical grid system. In the following, the term 'mesh' refers to a single topologically rectangular patch of cells and the term 'grid' refers to a collection of such patches. At the bottom of the hierarchy a set of coarse mesh patches delineates the computational domain. These patches form the grid G_0 and they are restricted such that there is continuity of grid lines between neighbouring patches. This domain may be refined locally by embedding finer mesh patches into the coarse grid G_0. These embedded patches form the next grid in the hierarchy, G_1. Each embedded patch is effectively formed by subdividing the coarse cells of the patches that it overlaps. The choice for the refinement ratio is arbitrary, but it must be the same for all the embedded patches. Thus, by construction, the grid G_1 also has continuity of grid lines. This process of adding grid tiers to effect local refinement may be repeated as often as desired, see figure 3.

From stability considerations, many numerical schemes have a restriction on the size of time step that may be used to integrate a system of equations. The finer the mesh, the smaller the allowable time step. Consequently, the AMR algorithm refines in time as well as space. More but smaller time steps are taken on fine grids than on coarse grids in a fashion which ensures that the rate at which waves move relative to the mesh (the Courant number) is comparable for all grid levels. This avoids the undesirable situation where coarse grids are integrated at very small Courant numbers
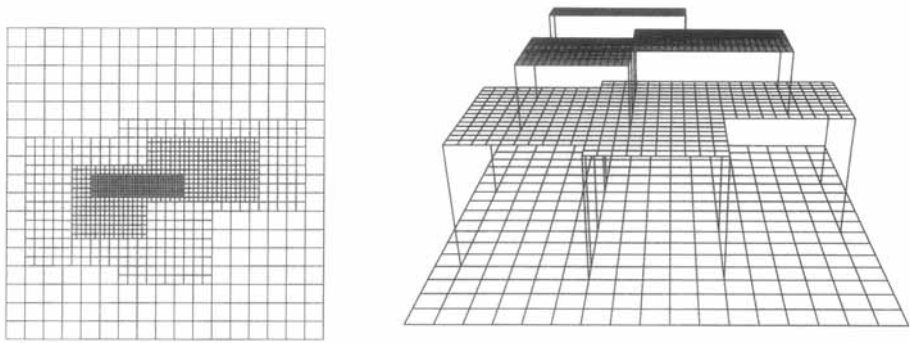
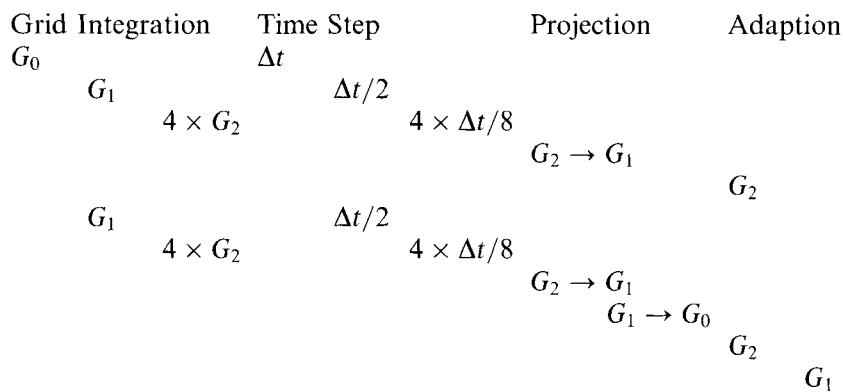FIGURE 3. The AMR algorithm employs a hierarchical grid system.

Grid	Integration	Time Step		Projection	Adaption
G_0		Δt			
	G_1	$\Delta t/2$			
	$4 \times G_2$		$4 \times \Delta t/8$		
				$G_2 \rightarrow G_1$	
					G_2
	G_1	$\Delta t/2$			
	$4 \times G_2$		$4 \times \Delta t/8$		
				$G_2 \rightarrow G_1$	
				$G_1 \rightarrow G_0$	
					G_2
					G_1

FIGURE 4. Grid operations are recursively interleaved (to be read from top to bottom).

given the time step set by the finest grid's stability constraints: some schemes (e.g. Lax–Wendroff) give poor accuracy for small Courant numbers.

The field solution on each grid is retained even in regions of grid overlap and so all grid levels in the hierarchy coexist. The order of integration is always from coarse to fine since it is necessary to interpolate a coarse grid solution in both time and space to provide boundary conditions for its overlying fine grid. The various integrations at the different grid levels are recursively interleaved to minimize the span over which any temporal interpolation need take place. Periodically, for consistency purposes, it is necessary to project a fine grid solution on to its underlying coarse grid. Figure 4 shows the sequence of integration steps and back projections for a three-level grid $\{G_0, G_1, G_2\}$ with refinement ratios of 2 and 4.

The integration of an individual grid is extremely simple in concept. Each mesh is surrounded by borders of dummy cells. Prior to integrating a grid, the dummy cells for every mesh patch in the grid are primed with data which are consistent with the various boundary conditions that have to be met. Each mesh patch is then integrated independently by an application-dependent black-box integrator that never actually sees a mesh boundary. Thus, in principle, any cell-centred scheme developed for a single topologically rectangular mesh can form the basis for the integration process.

In general it is necessary to adapt the computational grid to the changes in the evolving flow solution and so the grid structure is dynamic in nature. Monitor functions based on the local solution are used to determine automatically where refinement needs to take place to resolve small-scale phenomena (Quirk 1991). For
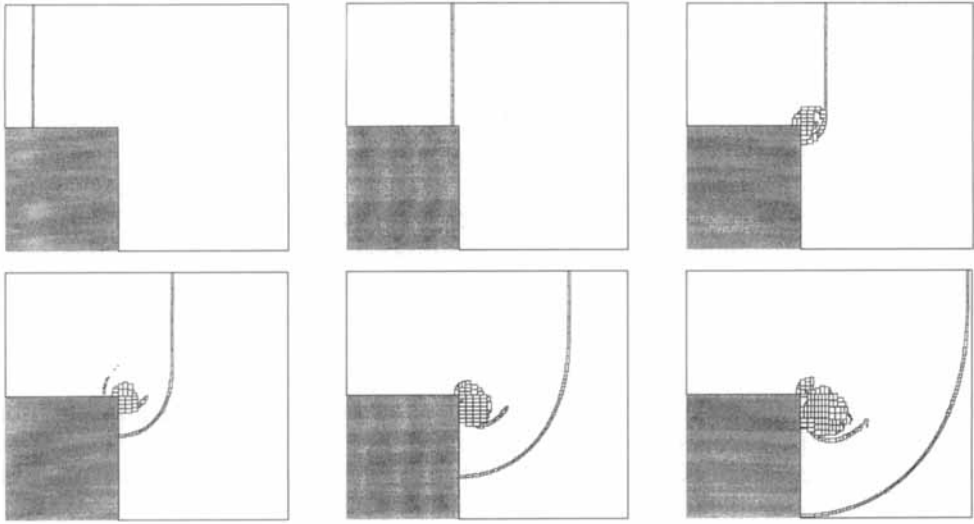
FIGURE 5. The AMR algorithm employs a dynamic grid system.

a simple example, figure 5 shows several snapshots taken from the simulation of a shock wave diffracting around a corner. Each snapshot shows the outlines of the mesh patches which go to make the finest grid. This grid clearly conforms to the main features of the flow, namely the diffracted shock front and the vortex located at the apex of the corner (Van Dyke 1982). Although the changes in grid structure shown here are dramatic, many adaptions have taken place between each frame (the mesh patches appear small, but each patch actually contains several hundred cells). A large number of small grid movements occurs because the adaption process dovetails with the integration process, see figure 4. Observe that the adaption always proceeds from fine to coarse so as to ensure that there is never a drop of more than one grid level at the edge of a fine grid to the underlying coarse grid. A grid adaption essentially produces a new set of mesh patches which must be primed with data from the old set of patches before the integration process can proceed. Where a new patch partially overlaps an old patch of the same grid level, for the region of overlap data may be simply shovelled from the old patch to the new patch. In regions of no such overlap, the required field solution is found by interpolation from the underlying coarse grid solution.

In a typical application the finest grid will contain several hundred mesh patches. Thus, the mesh patch is a sufficiently fine unit of data for efficient parallelism. The parallel AMR algorithm (Quirk 1996) is implemented using a Single Program Multiple Data (SPMD) model. Each processing node executes the basic serial algorithm (Quirk 1991) in isolation from all other nodes, except that at a few key points messages are sent between the nodes to supply information that an individual node deems to be missing, that is off-processor. For example, during the integration of a grid, the only point at which a processor needs to know about other processors is during the priming of the dummy cells. Whereas in a serial computation all data fetches are from memory, for a parallel computation some are from memory and some necessitate receiving a message from another processor. Each time the grid adapts, the algorithm generates a schedule of tasks that have to be performed so as to prime correctly the dummy cells of a given grid. If running in parallel, this schedule is

parsed to produce a schedule of those tasks that necessitate off-processor fetches, at which point, individual processors can exchange subsets of their fetch schedules, as appropriate, so that every node can construct a schedule of messages that it must send out at some later date. Thus, the priming process is carried out in two phases. First, all the local data fetches are performed as for the serial case. Second, each node sends out the data that has been requested of it. The node then waits for those data items it has requested. For each incoming message it can readily determine from its own schedules what to do with the off-processor data, and so the order in which messages arrive is unimportant. The adaption process and the back projection of the field solution between grid levels also necessitate sizeable amounts of communication; these are handled in a similar fashion to the priming of the dummy cells.

The problem of load balancing the AMR algorithm rests on determining the best distribution of the new patches amongst the processing nodes before the new field solution is interpolated from the old field solution. Currently, this is done using heuristic procedures (Quirk 1996) which bear strong similarities to classical 'bin packing' algorithms (Graham 1969) with the added complication that they must account for the communication costs of data transfer between nodes.

3.3. *Flow visualization images*

The plots shown in figures 7 and 9 depict the magnitude of the gradient of the density field,

$$
|\nabla \rho| = \left[\left(\frac{\partial \rho}{\partial x} \right)^2 + \left(\frac{\partial \rho}{\partial y} \right)^2 \right]^{1/2},
$$

and so may be viewed as idealized schlieren images. The density derivatives were computed using straightforward central-differencing, and the following nonlinear shading function, ϕ, was used to accentuate weak flow features:

$$
\phi = \exp \left(-k \frac{|\nabla \rho|}{|\nabla \rho|_{max}} \right).
$$

Here k is a constant that took the value 600 for the light fluid and 120 for the heavy fluid. Using a 24-bit colour graphics system, the grey shades outside the bubble were produced using the $\langle R, G, B \rangle$ triplet $\langle 230\phi, 230\phi, 230\phi \rangle$ and those within the bubble using $\langle 200\phi, 230\phi, 255 \rangle$. Thus the darker the image, the larger the density gradient.

Some realistically lit surface plots are also presented, e.g. figures 8 and 10. These are useful for determining the strengths of certain flow features, but lack of space prevents us from describing how they were produced.

4. Computational set-up

For our investigation of the dynamics of a shock–bubble interaction we have reproduced numerically two of the experiments performed by Haas & Sturtevant (1987). Namely, the interactions of a $M_S = 1.22$ planar shock wave, moving through air, with a cylindrical bubble of either helium or Refrigerant 22 ($CHClF_2$). Whereas the helium bubble is lighter than the surrounding air and so acts as a divergent acoustic lens, the R22 bubble is heavier and therefore acts as a convergent acoustic lens. As will be seen in §5, these two cases lead to very different flow behaviour.

In the experiments the bubbles were produced by inflating a cylindrical former whose walls were made from a very thin membrane of nitrocellulose. Thus good
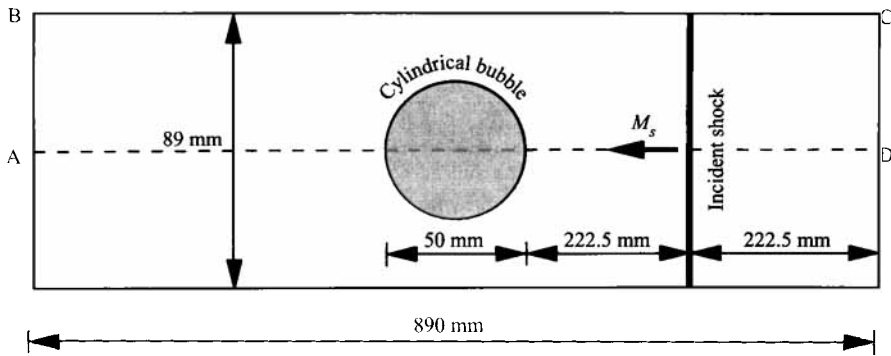
FIGURE 6. A schematic of the computational domain (not to scale).

control was exercised over the shape of the bubble and the resultant flows were almost two-dimensional, and so our computations which are two-dimensional can be expected to mimic the experiments fairly closely. Haas & Sturtevant produced three sets of results: (i) flow visualization in the form of spark shadowgraphs; (ii) velocities for certain key flow features; (iii) pressure traces measured at points downstream of the bubble along the axis of flow symmetry. We have produced similar sets of results from our simulations. However, it should be appreciated that the experimental results (shadowgraphs and velocities), unlike their computational counterparts, represent a compilation from a series of runs for each bubble case. Only a single spark shadowgraph could be taken from each run, and so the complete record was formed by repeating the experiment with different delay times to the exposure of the shadowgraph image. While this method produced excellent images, the accuracy of the velocity measurements necessarily suffered: since each measurement is derived from a sequence of images it is sensitive to the repeatability of the experiment. The general uncertainty in the velocity measurements is thought to be 11%, with the exception of a few instances for which it is thought to be as large as 30% (Haas & Sturtevant 1987).

A schematic of our computational set-up is shown in figure 6. We have assumed that the flow field is symmetric about the axis of the shock tube and so only the top half of the flow field (ABCD) was computed. The following boundary conditions were applied to the flow domain: sides BC and DA were treated as solid walls using a standard reflecting boundary procedure (Quirk 1991); the inflow along side CD was specified using the exact flow conditions behind the incident shock wave; zeroth-order extrapolation was used along the side AB. In practice neither the upstream nor the downstream boundary treatment is critical since no physical waves reach these boundaries. Of more relevance are the so-called 'start-up' errors which are generated when a shock smears to its natural profile given an exact discontinuity as starting conditions (Hillier 1991). It is for this reason that the incident shock was placed some distance to the right of the bubble so that these errors, which manifest themselves as a pair of low-frequency waves moving on the passive characteristics (Quirk 1991), would not have a chance to interfere with the shock–bubble interaction process.

All gas components were modelled as perfect gases; the appropriate values for the ratio of specific heats γ, the gas constant R, and the constant-volume specific heat capacity C_V, used for the simulations are given in table 1. The initial flow field was determined from standard shock relations given the strength of the incident shock wave ($M_S = 1.22$), taking the density and pressure of the quiescent flow

Gas Component	γ	R (kJ kg^{-1} K^{-1})	C_V (kJ kg^{-1} K^{-1})
air	1.4	0.287	0.72
R22	1.249	0.091	0.365
He	1.67	2.08	3.11
He+28% air	1.648	1.578	2.44

TABLE 1. Gas properties used in the simulations.

ahead of the shock to be unity. The bubble was assumed to be in both thermal and mechanical equilibrium with the surrounding air, therefore its initial density was simply R_{air}/R_{bubble}. For the helium bubble case, it was assumed that the contamination of helium with air was 28% by mass as indicated by Haas & Sturtevant (1987). As can be seen from table 1, this modifies the gas properties substantially. Given the experiences of Henderson *et al.* (1991), no attempt was made to model the effects of the membrane needed in the experiment to separate the two gas components. Therefore, ahead of the shock, each mesh cell was simply initialized with one of two states depending on whether its centre lay inside or outside the bubble.

The computational domain was discretized using 20 coarse mesh patches each of which formed a square of 50 by 50 cells. Additionally, two levels of refinement were used, both with a refinement factor of 4, to resolve flow details. Thus the effective grid resolution is equivalent to a uniform mesh of 16 000 by 800 cells with a spatial resolution of 0.056 mm. Both simulations were run as parallel computations on a small cluster of workstations (8 Sun Sparc10 Model 51s) and took two evenings each to complete. In this paper, we make no claims as to the computational efficiency of our numerical method, but it is sobering to consider that for the R22 bubble computation the equivalent uniform mesh calculation would require 3.26×10^{11} cell updates (16×1592 iterations on a mesh 16 000 by 800 cells). For our flow solver, a single processor of a CRAY Y-MP might manage one cell update every 10 μs in which case it would need 905 hours to run the simulation. Brute force computations on supercomputers do not represent a sensible option for investigations of shock wave phenomena.

5. Results and discussion: flow visualization

In this section we present a number of flow visualization images which reveal certain subtleties of the shock–bubble interactions which were not apparent from either the experiment or previous numerical studies.

5.1. *R22 bubble – convergent case*

Figure 7 shows a sequence of schlieren-type images from the simulation of the R22 bubble case; for comparison, the corresponding sequence of experimental images is also shown. Pleasingly, the simulation clearly reproduces all the salient features of the interaction. To bring out the quality of the simulation, and to show how it complements the experiment, we shall now describe this interaction in some detail. But first, to interpret correctly the images which follow, recall that the incident shock is moving from right to left and note that the original position of the bubble is marked by a light circle in the numerical images and by what looks like a dark circle with a T-shaped support in the experimental images.

Frame (*a*) of figure 7 shows a view of the R22 bubble some 55 μs after it is first hit

by the incident shock wave, from which it can be seen that the bubble has already undergone a slight deformation. What remains of the incident shock appears as two short vertical line segments near the top and bottom of the bubble. These segments are joined by a curved refracted shock which runs inside the bubble and a curved reflected shock which lies outside the bubble. A one-dimensional analysis for the precise moment the incident shock hits the bubble suggests that the reflected shock is 6.4 times weaker than the refracted shock. An appreciation of the relative strengths of these two waves can be gained from surface plots for the density and pressure fields (see figure 8a); the reflected wave is so weak it is hardly discernible. Here the refracted shock lags behind the incident shock because the sound speed inside the bubble is lower than that outside the bubble. Haas & Sturtevant (1987) observed that the refracted shock is slightly thickened at its two endpoints, but no explanation was given as to why this was so. From the surface plots it is clear that the refracted shock is slightly weaker at its endpoints, both the pressure and density surfaces appear slightly chamfered. Thus the thickening is indicative of a compression system that matches the pressure jumps between the weak and strong parts of the refracted shock.

As time moves on, the difference in sound speeds between the bubble and the surrounding air becomes more apparent, and by 115 μs (figure 7b) the refracted shock has folded such that two side limbs now run roughly normal to its central portion. The surface plots of the density and pressure fields for this time instant (figure 8b) reveal that each side limb varies markedly in its strength. In essence, for the flow inside the bubble, the air–R22 interface forms a concave ramp. Thus a series of compression waves is required to turn the flow through almost ninety degrees: each side limb is nearly horizontal and so the induced flow is vertical, but the induced flow behind the central portion of the refracted shock is largely horizontal. Observe that the two segments of the incident shock have started to diffract around the downstream half of the bubble, and that the bubble interface shows signs of incipient roll-ups where vorticity has been generated by the passage of the incident shock wave. Since the present flow model is inviscid, the development of these roll-ups will be controlled by vestigial numerical diffusion and so will depend upon the resolution of the computational grid, i.e. strictly speaking they are numerical artifacts. Nevertheless such roll-ups are qualitatively realistic, and as discussed in §2 it is doubtful whether a viscous flow model would improve matters since a prohibitively fine mesh would be required to resolve the appropriate scales accurately.

By 135 μs the system of compression waves which turns the flow around each of the two bends in the refracted shock has steepened and is clearly visible in the surface plots for the density and pressure fields (figure 8c). Thus the refracted wave does not extend beyond its junction with the side limbs as was suggested by Löhner *et al.* (1988). Whilst the thickening of the refracted wave shows up much more starkly in the experimental shadowgraphs than it does in the numerical schlieren images, it should be remembered that an experimental shadowgraph represents an integration of the curvature of the density field across the entire width of the shock-tube facility used to perform the experiment. Consequently, any small three-dimensionality in the flow field will subtly alter the recorded image in ways that are not always easy to fathom. Here we believe the exaggerated thickening is an experimental artifact, because, referring to figure 7(c), within the upper of the two thickened limbs that appear in the experimental image it is just possible to make out a line which matches the front shown by the numerical image. However, as noted by one of the referees, the precise cause of the artifact might also lie with an optical distortion in the shadowgraph
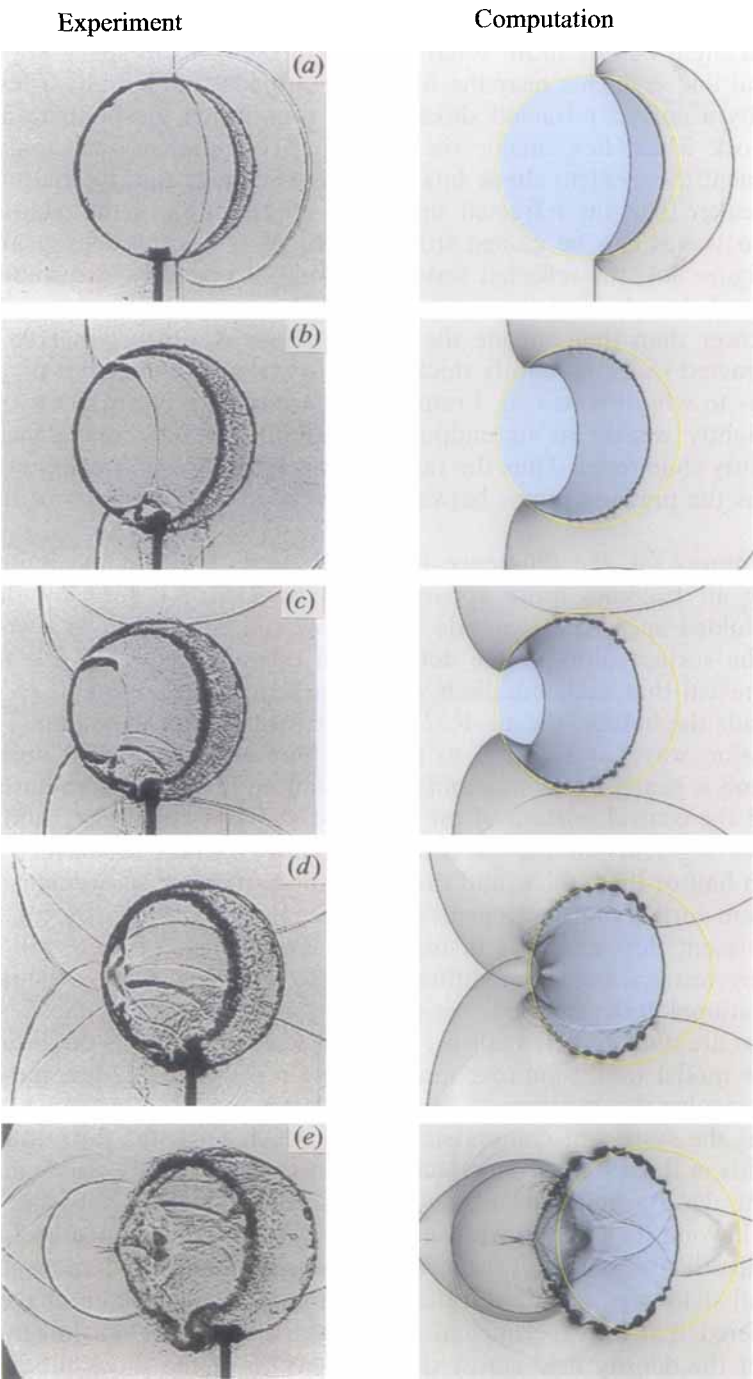
Experiment   Computation

FIGURE 7(*a–e*). For caption see facing page.

system, or with the fact that caustics formed owing to the large deflection of light by the gradients in refractive index.

Other artifacts of the experiment are much more obvious and do not cause undue confusion. For example, it is clear from figure 7(*c*) that the bubble's support structure
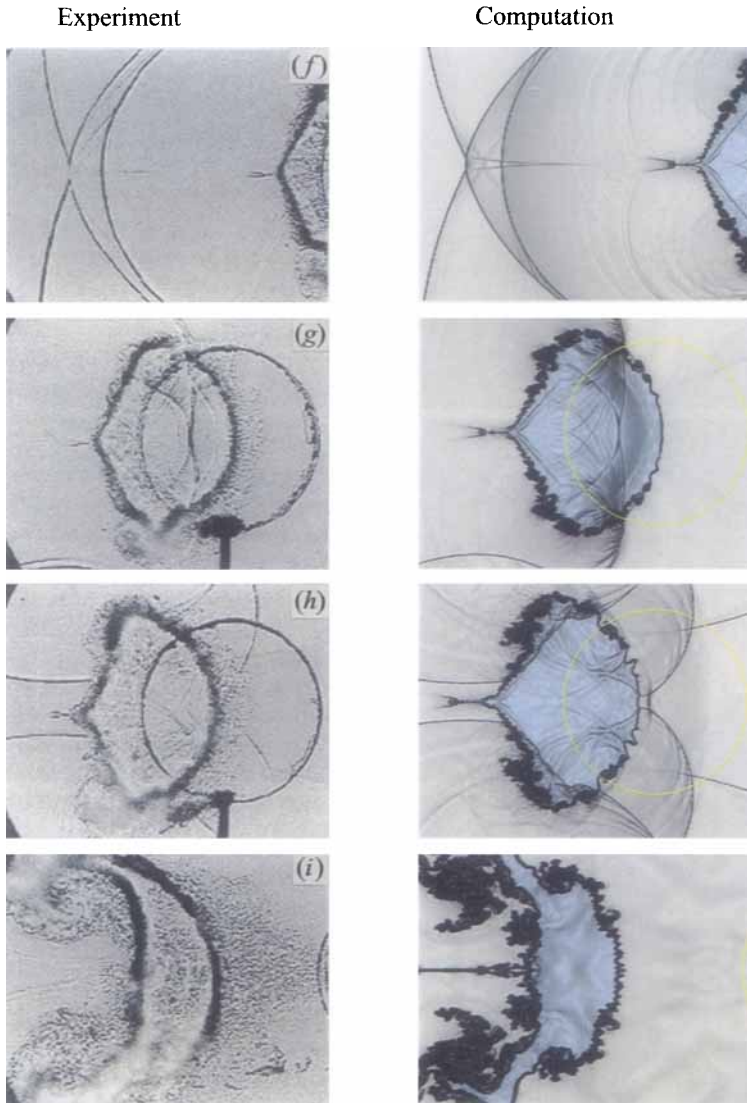
Experiment   Computation

FIGURE 7. Numerical schlieren images and experimental shadowgraphs (Haas & Sturtevant 1987) from the interaction of an $M_S = 1.22$ shock wave moving from right to left over an R22 cylindrical bubble. Times: (a) 55 µs, (b) 115 µs, (c) 135 µs, (d) 187 µs, (e) 247 µs, (f) 318 µs, (g) 342 µs, (h) 417 µs, (i) 1020 µs. Experimental images ©Cambridge University Press 1987. Reprinted with permission of Cambridge University Press.

gave rise to a number of spurious waves, as did the walls of the shock tube, but we model reflections from the tube's walls and so these particular waves also appear in the numerical images. Looking beyond the present study, it would be interesting to perform a series of simulations to determine the influence such blockage effects have on the dynamics of the interaction process.

Figure 7(d) shows that by 187 µs the refracted shock has been focused down to almost a point. The increase in peak pressure caused by this focusing is seen in the corresponding surface plots (figure 8d); at this time, the peak pressure is 2.1 times larger than the expected pressure behind an $M_S = 1.22$ shock wave. Outside the

Pressure   Density
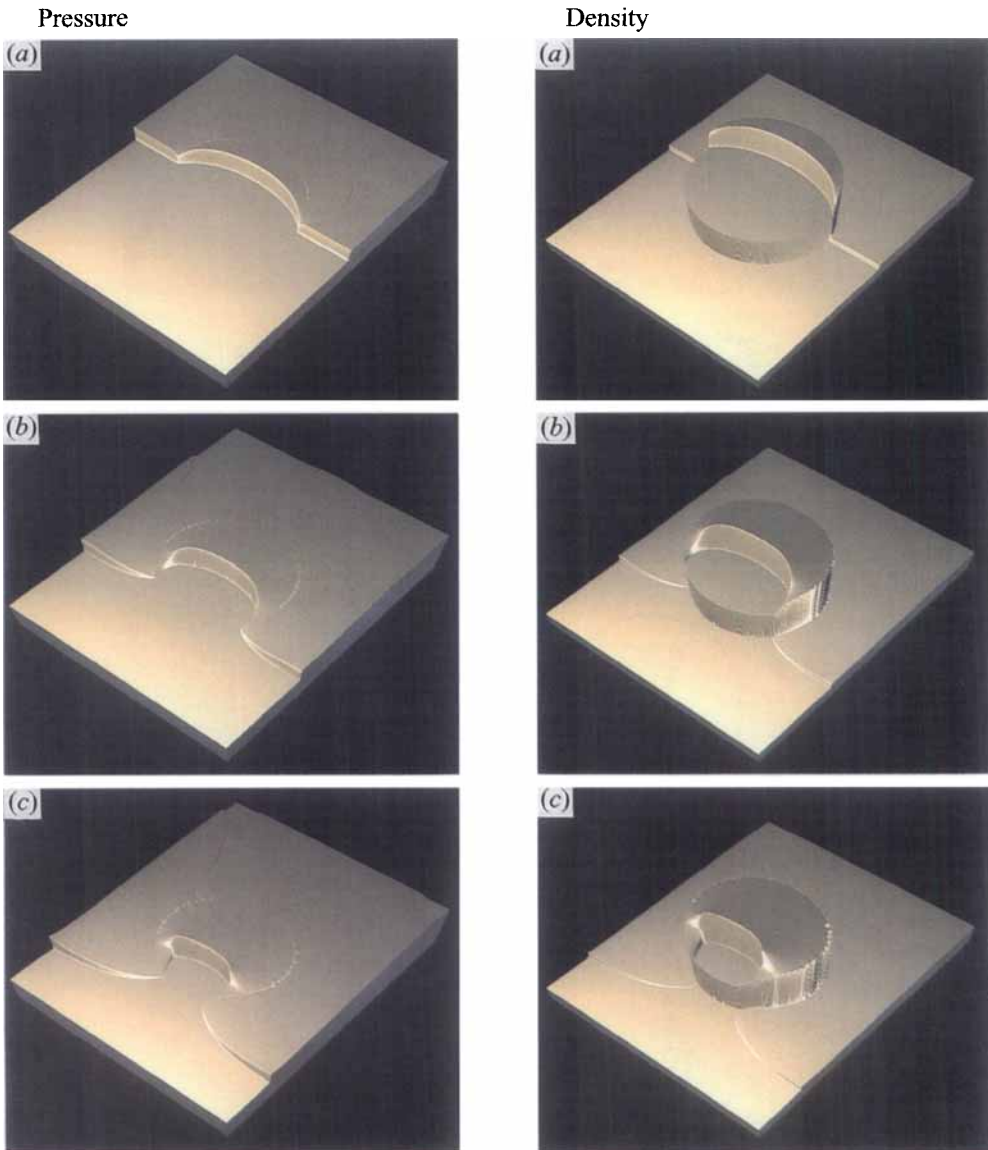
FIGURE 8(*a–c*). For caption see facing page

bubble, the top and bottom segments of the incident shock wave have now crossed, following their diffraction around the downstream half of the bubble, and two weak contact discontinuities are now visible. These contacts separate regions of fluid that have been induced into motion by either the diffracted part or the undisturbed part of the incident shock wave. The reflected shocks from the top and bottom walls of the shock tube have now started to pass through the bubble. Again these shocks lag behind their counterparts outside the bubble because of the difference in the sound speeds between the light and heavy fluids. The roll-ups along the bubble interface have become much more pronounced and are very prominent in the surface plot for the pressure field where they appear as tiny scallops (figure 8*d*). Interestingly the passage of the top and bottom reflected shocks through the corrugated bubble interface has

Pressure   Density
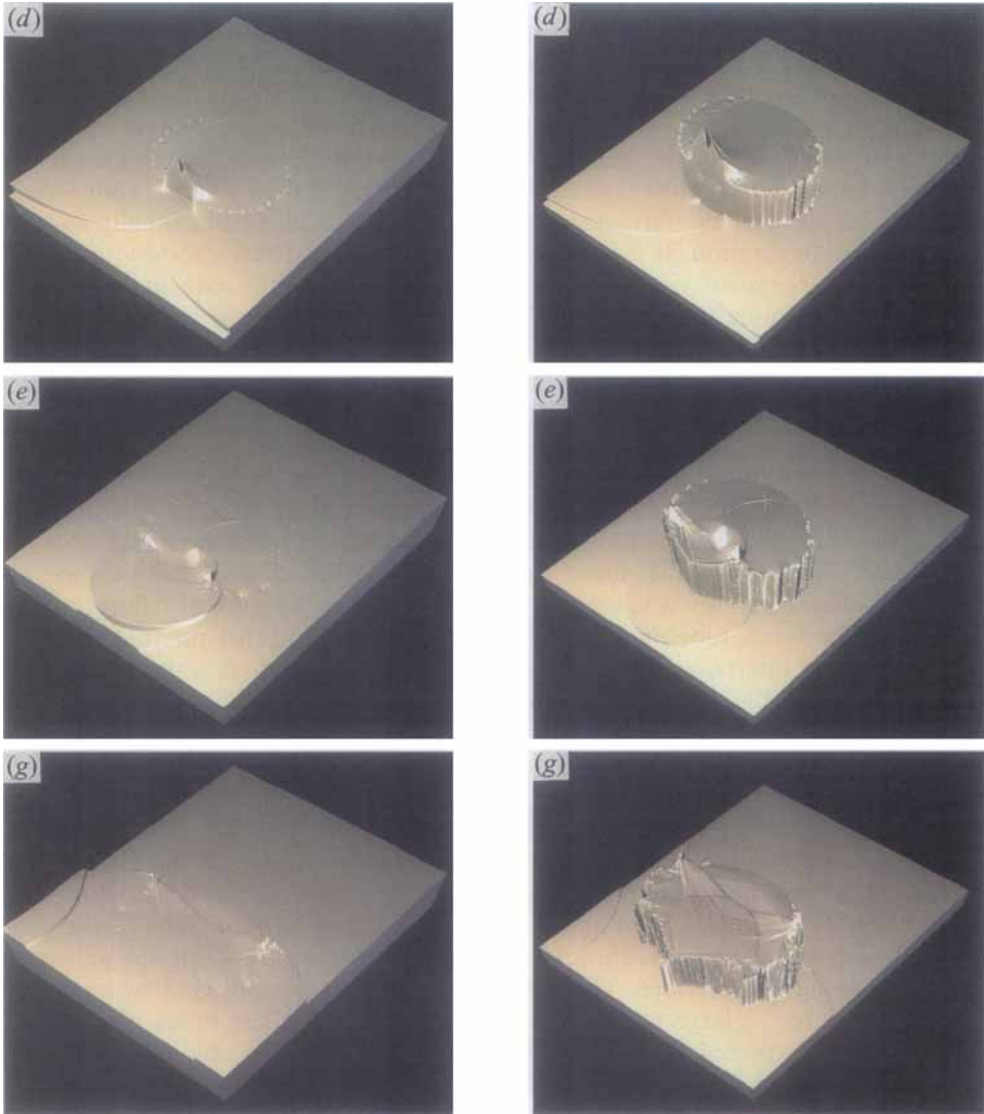
FIGURE 8. Surface plots of the density and pressure fields for the interaction of an $M_S = 1.22$ shock wave with an R22 cylindrical bubble. Times: (a) 55 µs, (b) 115 µs, (c) 135 µs, (d) 187 µs, (e) 247 µs, (g) 342 µs.

given rise to a number of cylindrical acoustic waves which then recombine to form a shock in a manner reminiscent of Huygen's front reconstruction.

Once the refracted shock has been focused it emerges from the downstream interface to become a transmitted wave which is cylindrical (figure 7e). The downstream interface of the bubble necessarily aligns itself with the resultant velocity field which is almost radial and so it takes on a wedge-like shape. Additionally the cylindrical transmitted wave is at the stage of catching up the two diffracted segments of the incident shock front. Although the agreement between experiment and computation is poor at this time, it is worth remembering that each shadowgraph was produced from a

separate experimental run. Therefore, the fact that we are generally able to match our numerical schlierens so closely to the shadowgraphs is testimony to the repeatability of the experiment. In this one instance, it would appear that the experimental run was relatively poor and that the gross features of the computation are correctly positioned.

If there is any criticism of the simulation, it should be directed at a few subtle shortcomings on the small scale. For example, the two-pronged feature emanating from the left-hand side of the bubble (figure 7e onwards), seems unduly exaggerated in our simulation. This feature is caused by a narrow jet of fluid which is shot forward during the focusing of the refracted wave. As yet, we cannot categorically state the cause of this exaggeration. It is probably due to the lack of real viscosity in the flow model. In the experiment viscosity causes the jet to spread thus reducing its range of influence. In the simulation, which is inviscid, any spreading of the jet is simply down to residual numerical diffusion. Given the resolution of the present computation, this residual diffusion is very small and so the spreading of the jet will be underdone giving it an exaggerated range of influence. However, it is conceivable that the exaggeration is yet another obscure numerical failing of the type catalogued by Quirk (1994).

By 342 μs the bubble has moved appreciably from its original position and it has started to elongate (figure 7g). Inside the bubble there is a backward moving shock which was born from the internal reflection of the refracted shock from the downstream interface. In the numerical image a number of weaker waves are also apparent, caused by waves which pass through the bubble because of reflections from the walls of the shock tube and which subsequently lead to other internal reflections from the bubble interface. Outside the bubble, the transmitted wave has reflected from the walls of the shock tube, and as can be seen from the surface plots for this time (figure 8g), spikes in the pressure and density fields still persist where the transmitted wave intersects the bubble interface. The apparent feathering of the transmitted shock is due to its passage over what is now a corrugated surface given the many roll-ups along the bubble interface.

The internally back-reflected shock wave eventually emerges from the upstream interface to become a backscattered wave (figure 7h), while the waves resulting from the reflection of the transmitted shock from the top and bottom walls of the shock tube in their turn start to pass through the bubble, further promoting the generation of vorticity along the interface. The bubble continues to elongate and by much later times it evolves into a large vortex pair (figure 7i). For these late times, when viscous effects might be expected to dominate proceedings, it is remarkable that an inviscid simulation gives such qualitatively good agreement with experiment.

5.2. *Helium bubble – divergent case*

Figure 9 shows a sequence of schlieren-type images from the simulation of the helium bubble case; again the simulation reproduces all the features of the interaction process.

Figure 9(a) shows a view of the helium bubble 32 μs after it is first hit by the incident shock wave. As before, there is a curved refracted shock which lies inside the bubble; however, since the helium has a higher sound speed than the surrounding air ($a_{air}/a_{He} = 0.35$), the refracted shock now moves ahead of the incident shock. Outside the bubble, the curved reflected wave is neither a simple shock nor a simple expansion wave. A one-dimensional Riemann problem analysis suggests that the reflected wave should be a weak expansion (the density jump across this wave is 19% of the density jump between the undisturbed bubble and the surrounding air). Indeed, the surface plots for the pressure and density field confirm that this expectation is true near the axis of flow symmetry (figure 10a). However, away from this axis there is very little

deformation of the bubble and the point of reflection acts as a solid surface giving rise to a reflected shock. Behind this shock there is an expansion system which accounts for the lower pressure to be found behind the rest of the reflected wave due to the collapse of the bubble.

The difference in sound speeds between the bubble and the surrounding air becomes more apparent by 52 μs (figure 9*b*) where the refracted shock has run well ahead of the incident wave. A four-shock configuration has formed which Henderson *et al.* (1991) have termed twin regular reflection-refraction (TRR). A schematic for this shock configuration is shown in figure 11. Given the relative positions of the four shocks no discernible contact discontinuity emanates from their intersection point as would be expected in the general case, although one does become visible by 72 μs (figure 9*d*). Around 62 μs (figure 9*c*) the refracted wave emerges from the left-hand side of the bubble to become the transmitted wave and the resultant internally reflected wave appears as two cusps. As can be seen from figure 9(*d*), this reflected wave is convergent and is being focused along the axis of the bubble but the local increase in pressure is quite small (figure 10*d*). By 82 μs (figure 9*e*) the internally reflected waves have crossed and are now diverging; here they appear as a small loop. The two branches of the transmitted shock have also now crossed. At 102 μs (figure 9*f*), along the axis of flow symmetry the side shock and the transmitted shock have almost merged. Meanwhile, both the original reflected wave and the transmitted shock have reflected from the walls of the shock tube, and as can be seen from figure 10(*f*) such spurious reflections can lead to large increases in local pressure. Here the foot of the incident shock, where it meets the shock tube's walls, is reinforced substantially. This spike then proceeds to move away from the wall and eventually interacts with the bubble. At this time, what remains of the incident shock has just started to diffract around the downstream side of the bubble, and the internally reflected wave has emerged from the upstream interface as a weak backscattered wave. This has resulted in a very weak internally reflected wave, so weak in fact that it does not appear in the experimental images. As time moves on, the bubble becomes kidney shaped and spreads laterally in the process (figure 10*g*). This change in shape is driven by vorticity generated at the edge of the bubble due to the passage of the shock which induces a jet of air along the axis of flow symmetry. When this jet impinges on the air at the downstream edge of the bubble, which is less easily displaced than the lighter helium, it spreads laterally and the bubble forms a pair of distinct vortical structures (figure 10*i*).

6. Results and discussion: velocities

The results from the previous section clearly indicate that the present simulations are qualitatively correct; however, any serious numerical investigation should contain some form of validation exercise. Here, this included a quantitative check on the velocities of several prominent flow features. For each simulation, the positions of certain features were digitized from a sequence of schlieren-type images. Using these measurements, x, t diagrams were then constructed to find the velocities. Whereas the experimentally measured velocities had an estimated uncertainty of 11%, here the uncertainty is much smaller. A shock might be smeared over 3 mesh cells, therefore given the resolution of the computational grid its location can be determined to within ±0.17 mm. This equates to an uncertainty of less that 1% in the worst-case velocity measurement. The uncertainty in velocity due to conservation errors is also small at less than 3%.
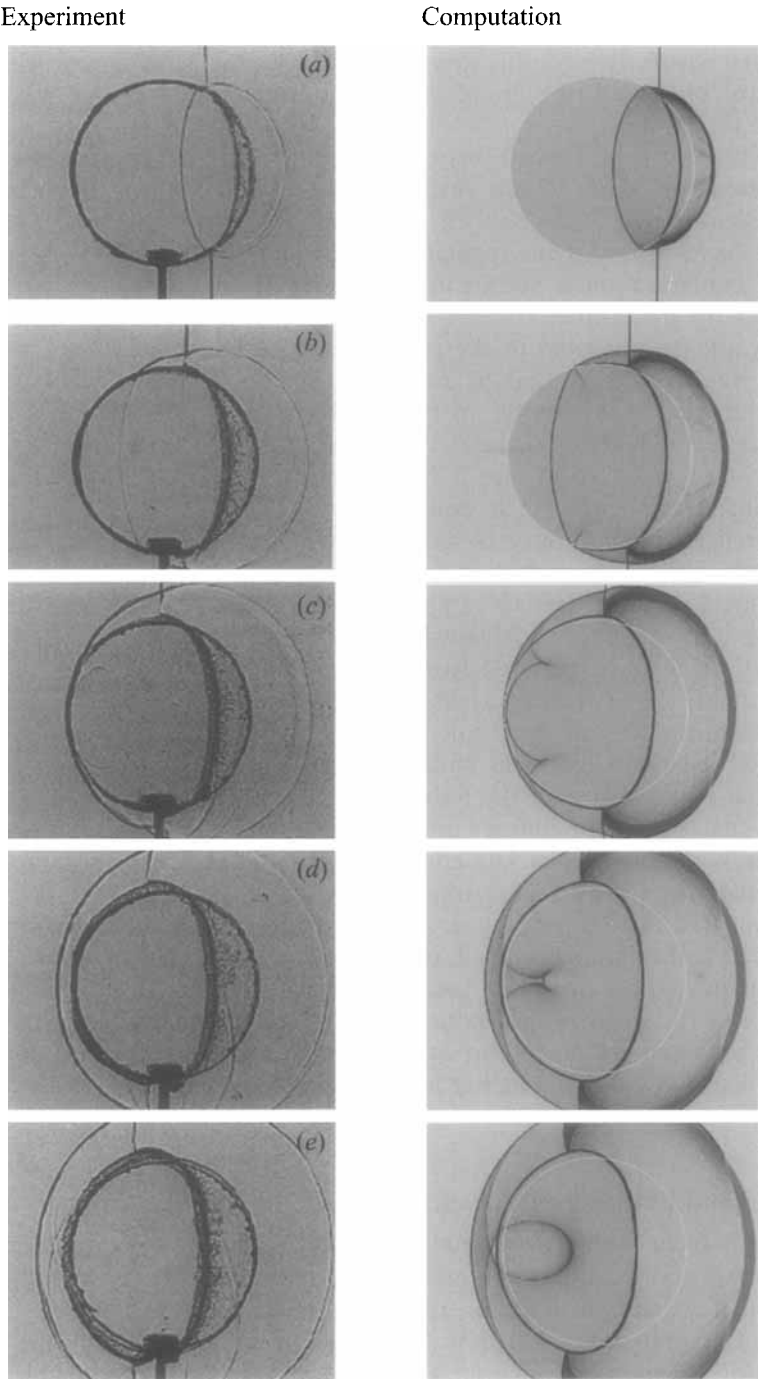
Experiment   Computation

FIGURE 9(*a–e*). For caption see facing page.

6.1. *R22 bubble – convergent case*

The x, t diagram for the R22 bubble case is shown in figure 12, together with a schematic which identifies the various flow features that have been digitized. A comparison of the computed velocities with their experimentally measured counterparts
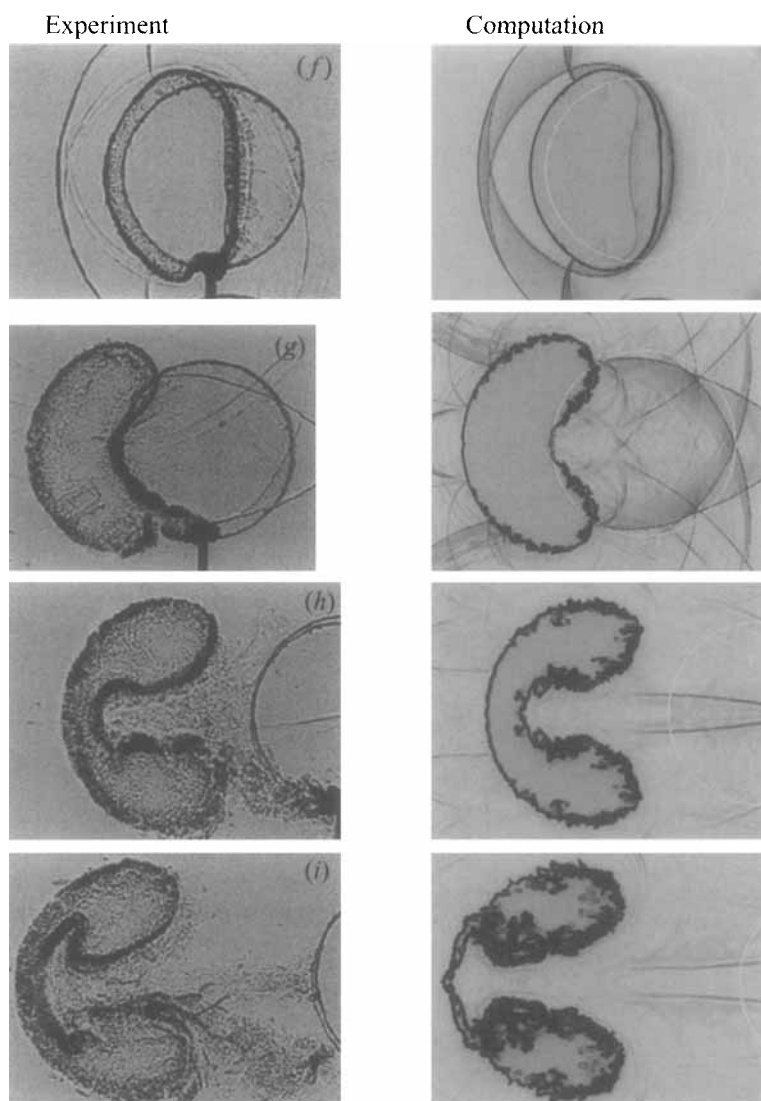
Experiment   Computation

FIGURE 9. Numerical schlieren images and experimental shadowgraphs (Haas & Sturtevant 1987) from the interaction of an $M_S = 1.22$ shock wave moving from right to left over a helium cylindrical bubble. Times: (a) 32 μs, (b) 52 μs, (c) 62 μs, (d) 72 μs, (e) 82 μs,(f) 102 μs, (g) 245 μs, (h) 427 μs, (i) 674 μs. Experimental images ©Cambridge University Press 1987. Reprinted with permission of Cambridge University Press.

(Haas & Sturtevant 1987) is given in table 2. The agreement between the two sets of results lies well within the given 11% experimental error; the worst case (V_R) is just 5.8%. Moreover the discrepancy is mitigated by the fact that the wave fronts do not move with constant velocity. Figure 12 contains slight accelerations and decelerations which are swamped by the scatter in the corresponding experimental x, t diagram. For example, the refracted wave starts off with a velocity of 242 m s^{-1} but accelerates to 265 m s^{-1} by $t = 160$ μs, giving an average of 254 m s^{-1}. Similarly, the upstream interface of the bubble decelerates from 84 m s^{-1} to 61 m s^{-1} over the same period, giving an average of 74 m s^{-1} (see figure 17a).

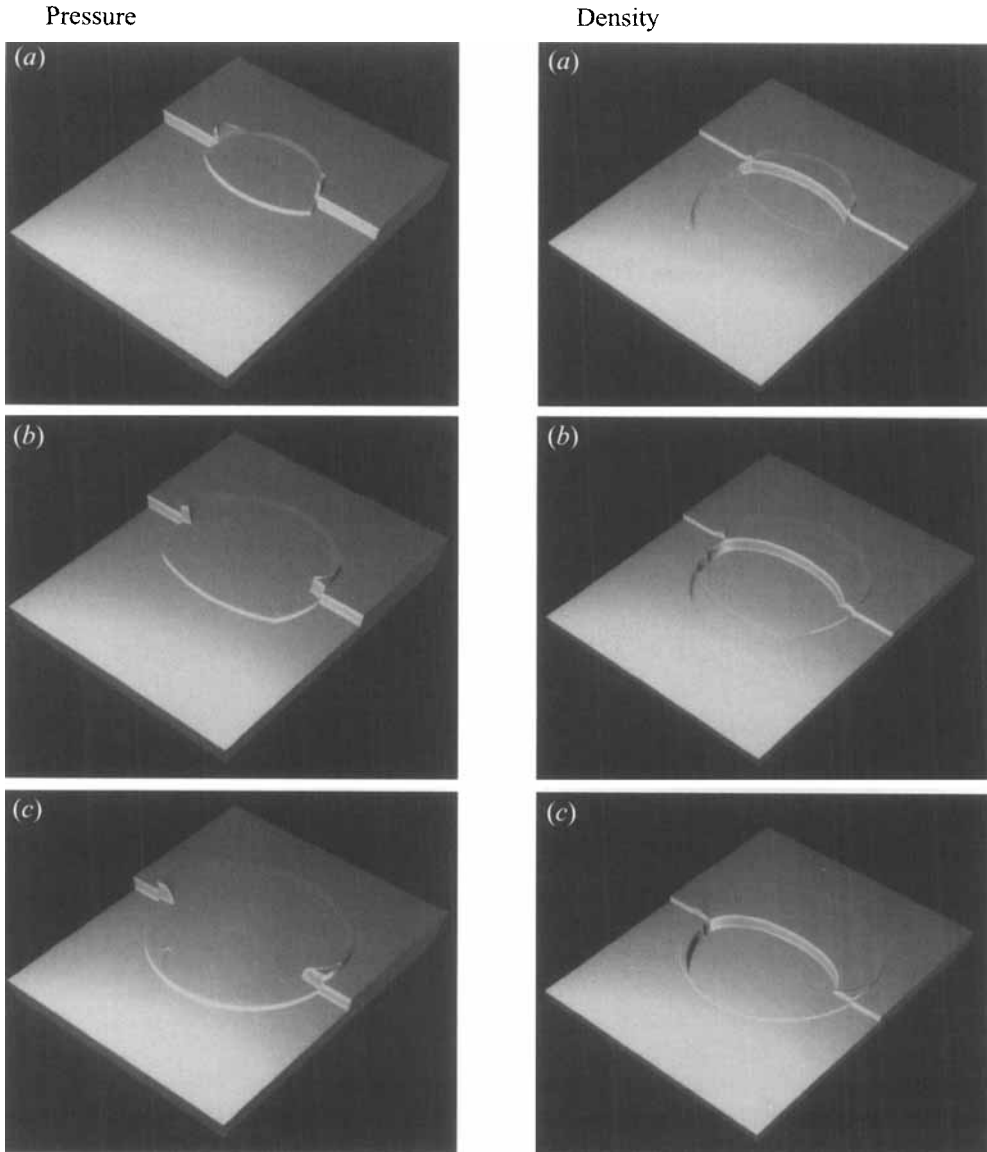Overall, the general agreement between the two sets of velocities confirms the

Pressure   Density

FIGURE 10(*a–c*). For caption see facing page.

experimentalists' view that the contamination of R22 by air was so small (they estimated it at 3.4% by mass) as to be negligible. Note that we have chosen to ignore the large discrepancy for V_{di} since the experimental value appears to have been tabulated incorrectly; the experimental x, t diagram indicates that V_{di} is close to 130 m s^{-1} which is in fair agreement with the computation.

6.2. *Helium bubble – divergent case*

The x, t diagram for the shock interaction with the helium bubble is shown in figure 13, and a comparison with experiment is made in table 3. As with the R22 case, the two sets of results are in close agreement. However, the effects of air contamination are now significant. As detailed in §4, we have assumed that the contamination of
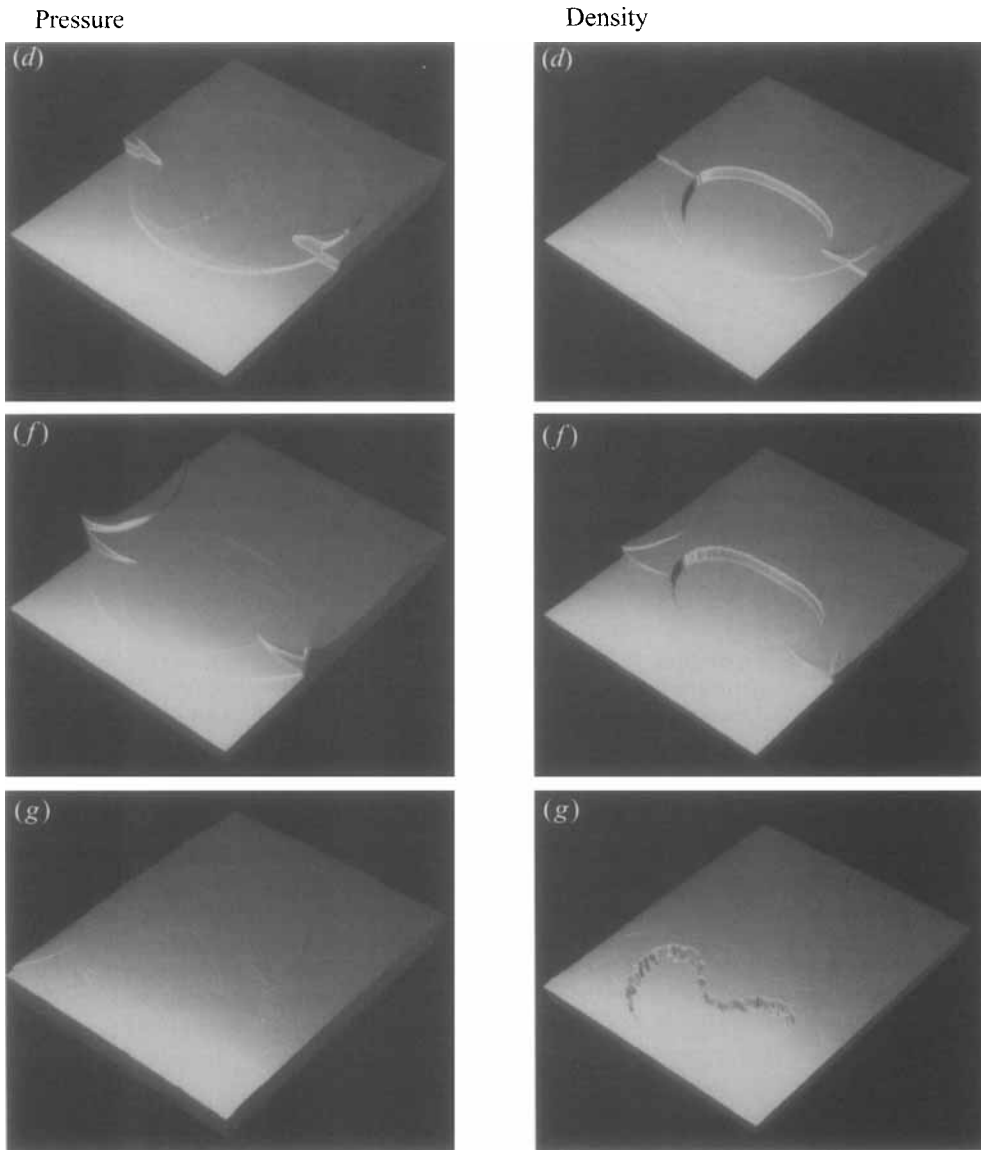
Pressure   Density

FIGURE 10. Surface plots of the density and pressure fields for the interaction of an $M_S = 1.22$ shock wave with an He cylindrical bubble. Times: (a) 32 μs, (b) 52 μs, (c) 62 μs, (d) 72 μs, (f) 102 μs, (g) 245 μs.

helium by air is 28% by mass. If no account is taken of contamination, the velocity results are very different even though the flow remains qualitatively similar. For example, the velocity V_R with 28% contamination is 943 m s^{-1}; alternatively, with zero contamination it is found to be 1073 m s^{-1}; an increase of 13.5%. The correction for contamination necessarily assumes that the air and helium are homogeneously mixed. Since this would not have been the case in the experiment, our correction can only be viewed as accounting for the gross affects of contamination.
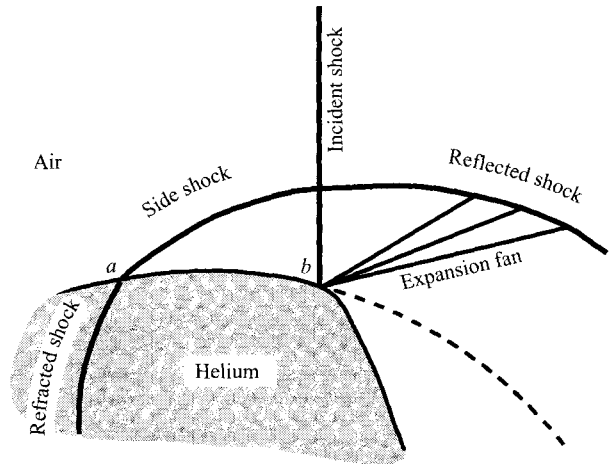
FIGURE 11. Schematic for twin regular reflection-refraction (TRR).

Velocity	V_s	V_R	V_T	V_{ui}	V_{uf}	V_{di}	V_{df}
Computation	420	254	560	74	90	116	82
Experiment	415	240	540	73	90	78	78
% Discrepancy	+1.2	+5.8	+3.7	+1.4	+0.0	N/A	+5.1

TABLE 2. A comparison of the computed velocities for the R22 cylinder case with those measured experimentally by Haas & Sturtevant (1987); for notation, see figure 12.

Velocity	V_s	V_R	V_T	V_{ui}	V_{di}	V_j
Computation	422	943	377	178	146	227
Experiment	410	900	393	170	145	230
% Discrepancy	+2.9	+4.8	−4.1	+4.7	+0.7	−1.3

TABLE 3. A comparison of the computed velocities for the He cylinder case with those measured experimentally by Haas & Sturtevant (1987); for notation, see figure 13.

7. Results and discussion: pressure traces

In addition to producing shadowgraphs, Haas & Sturtevant recorded pressure histories at several stations along the axis of flow symmetry to build up a more complete picture of the shock–bubble interaction process. For example, in the heavy bubble case, they noted that the diffracted wave generated a smooth pressure disturbance at a measuring station 3 mm downstream of the initial bubble position, and not a discontinuous disturbance as might be expected from a shock wave. In fact, as was shown in §5, the diffracted front barely constitutes a shock wave in the vicinity of the bubble interface: the surface plots in figure 8 reveal that along the interface the pressure field ramps up gradually behind the diffracted wave and is not discontinuous, hence the smooth nature of the measured disturbance.

Although the experimental pressure traces only provide a local view of events and so are not as informative as the present pressure surfaces, it was hoped that they could be used to provide further quantitative evidence as to the accuracy of the simulations. Unfortunately, the traces cannot be relied upon to provide an accurate benchmark
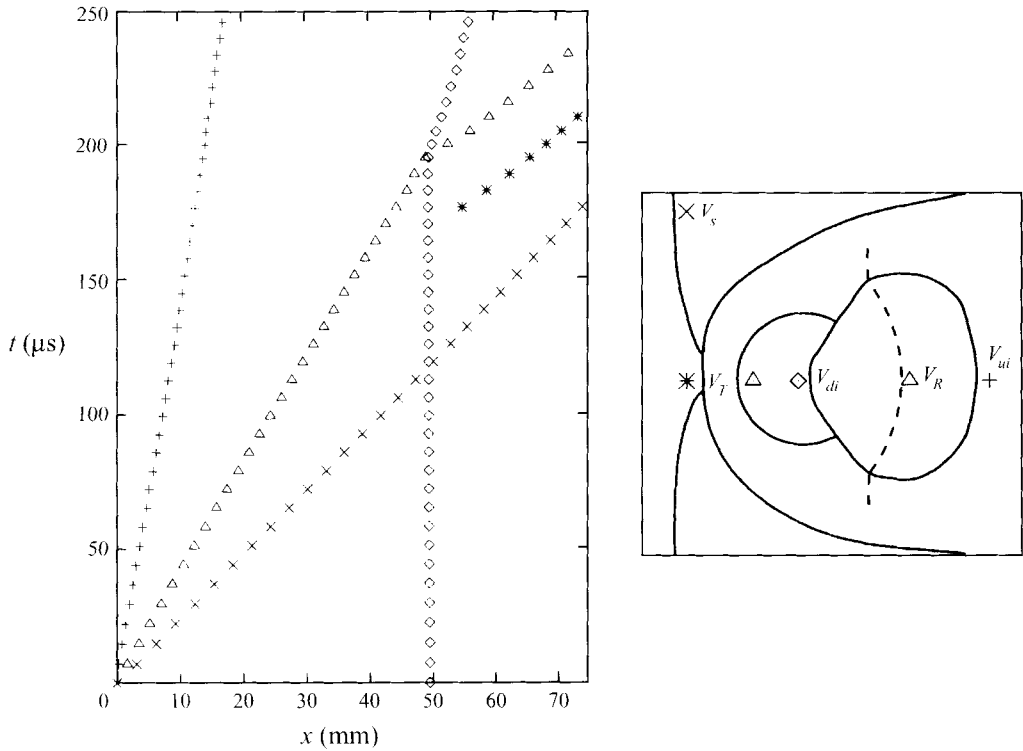
FIGURE 12. x,t diagram for the R22 cylinder case with a schematic showing the points used to construct the diagram: V_s – incident shock; V_R – refracted shock; V_T – transmitted shock; V_{ui}, V_{uf} – upstream edge of bubble, initial and final times (relative position of V_{uf} is the same as V_{ui}); V_{di}, V_{df} – downstream edge of bubble, initial and final times (relative position of V_{df} is the same as V_{di}).

since the measuring process was invasive. A pressure transducer was mounted on a movable endwall placed within the shock tube (Haas & Sturtevant 1987), thus the transducer actually measured the pressure disturbances for waves reflecting off the endwall and not the local pressure as desired. Consequently, the transducer would be expected to produce readings on the high side. This agrees with our findings. For example, the experiment gave the peak pressure in the heavy bubble case as 7.7 bar, but the simulation suggests that it is close to 5.1 bar. Also, the experiment indicated that the long-time pressure, once all the disturbances have died away, this pressure should be close to the pressure behind a $M_S = 1.22$ shock wave which is only 1.56 bar (the simulation gave the long-time pressure to be 1.6 bar). Here, the numerics provide a quantitative assessment of the errors introduced by the practicalities of the experimental set-up. Thus it seems the invasive pressure readings were 37–51% too high.

Although we cannot make a useful comparison with experiment, for completeness we present the numerical pressure traces from the heavy bubble case, see figure 14 (cf. figure 16 of Haas & Sturtevant 1987).

8. Results and discussion: vorticity generation

Although it takes us beyond the main purpose of this paper, we can use our numerical results to make some observations which are pertinent to several recent
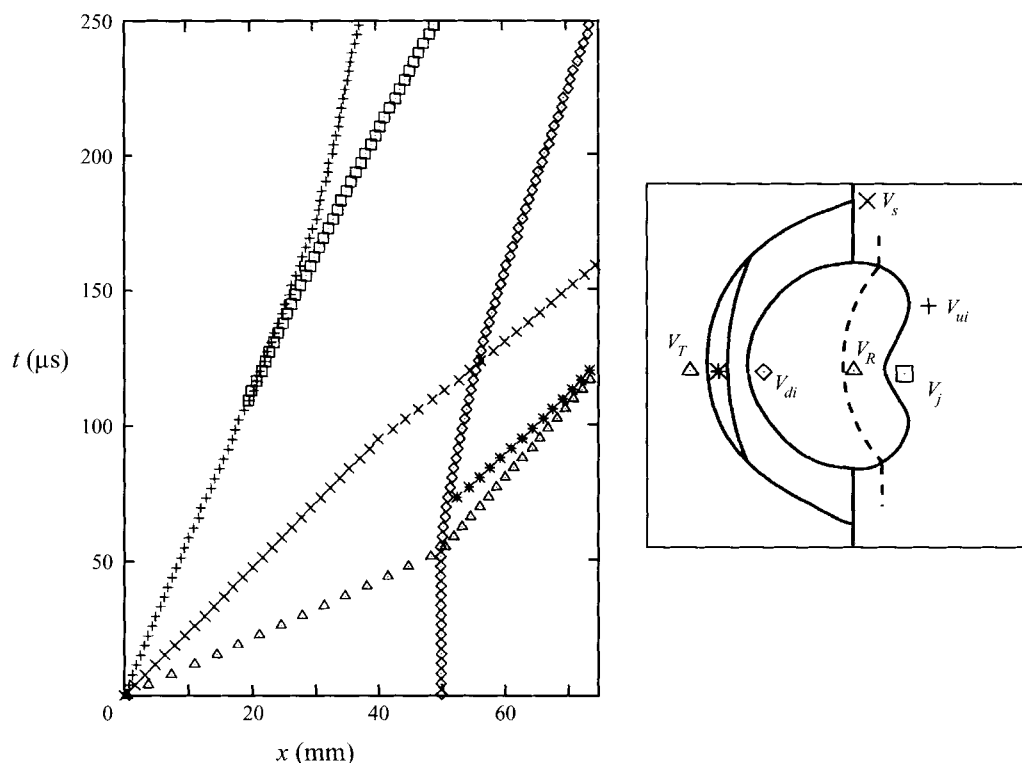
FIGURE 13. x, t diagram for the He cylinder case with a schematic showing the points used to construct the diagram: V_s – incident shock, V_R – refracted shock, V_T – transmitted shock, V_{ui} – upstream edge of bubble, V_{di} – downstream edge of bubble, V_j – air jet head.

studies on shock-induced mixing: the present two-dimensional unsteady flow is analogous to a three-dimensional steady flow that has been proposed as a mechanism to enhance mixing of air and fuel in supersonic combustions systems (Marble *et al.* 1987; Drummond & Givi 1994). Essentially, vorticity which is impulsively generated by the passage of the shock through the bubble drives a mixing process reminiscent of the Richtmyer–Meshkov instability (Richtmyer 1960; Meshkov 1970; Rupert 1992).

Recall that the vorticity evolution equation, which is derived from the curl of the momentum equation, contains the baroclinic torque term

$$\nabla \times \left(\frac{1}{\rho} \nabla p \right).$$

This term may be recast so as to write the vorticity equation in the form

$$\frac{D\omega}{Dt} = \quad \dots \quad + \frac{1}{\rho^2} \nabla \rho \times \nabla p,$$

from which it can be seen that vorticity is produced whenever there is a misalignment in the gradients of the density and pressure fields (Shercliff 1977). In the case of a shock–bubble interaction, such a misalignment occurs because the propagating shock wave imposes a local pressure gradient which is largely independent of the local density gradient imposed by the bubble inhomogeneity.

Several authors have devised approximate analytic expressions to predict the circulation produced by an isolated shock–bubble interaction so as to have a means of
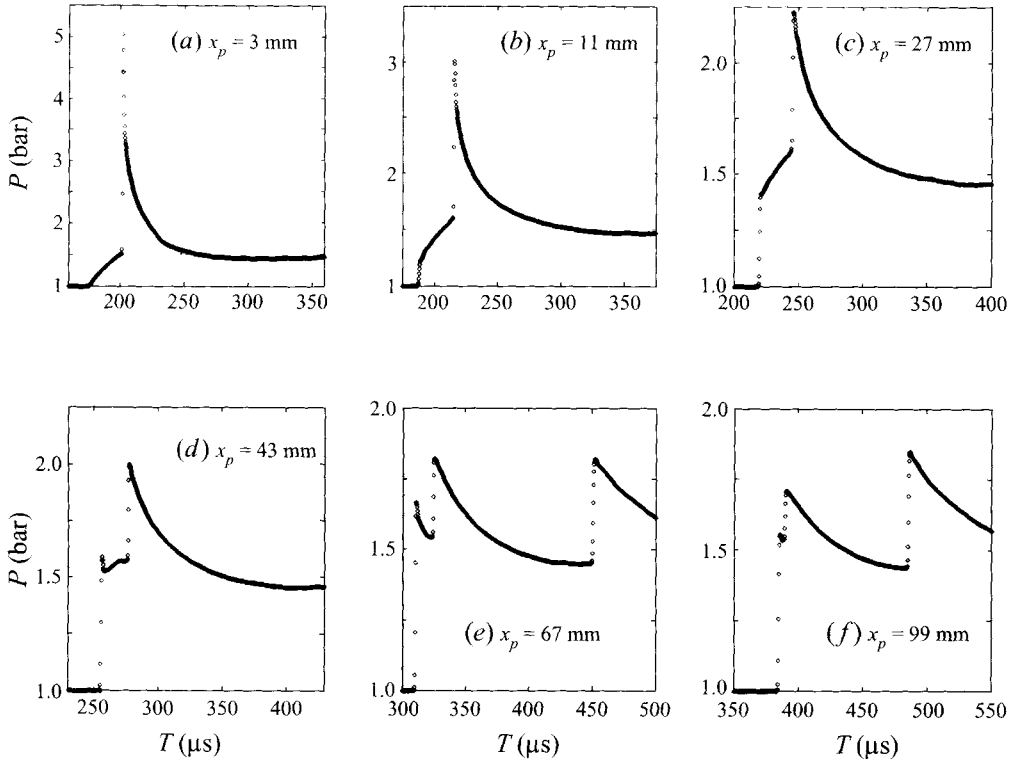
FIGURE 14. Pressure histories at several stations downstream of the R22 cylinder.

gauging the effectiveness of the associated late-time mixing. Typically, this is done by making enough simplifying assumptions that the baroclinic torque can be integrated over the bubble for the duration of the interaction (e.g. Picone & Boris 1988 and Yang *et al.* 1994), although Samtaney & Zabusky (1994) adopt a more sophisticated approach and compute vorticity directly from the local velocity field found by shock-polar analysis. Various claims are made for these models (which are henceforth referred to as PB, YKZ and SZ respectively) based on their respective abilities to provide circulation predictions close to those found by numerical simulations. For example, although mathematically approximate, the YKZ model is claimed to retain the essential features of the interaction process, since across a range of cases its discrepancy with simulation is less than 15%. However, our simulations indicate that this and other claims made for these models are debatable.

Consider the present helium bubble case. Both the PB and YKZ models assume that the pressure gradient responsible for the baroclinic torque remains constant and acts horizontally throughout the interaction, and that vorticity production continues for the time it takes the incident shock to traverse the bubble. But a plot of circulation as a function of time (figure 15*b*) reveals that the circulation bottoms out around $t = 60$ μs which is just short of the time when the refracted wave emerges from the bubble (see figure 9*c*). Thus both models overestimate the duration of vorticity production by more than a factor of 2, since $V_R/V_I = 2.23$. Somewhat fortuitously this gross error appears to be compensated by other errors in the assumptions. Firstly, the relevant pressure gradient does not remain constant but significantly weakens during the interaction (see figure 10*a, f*). Secondly, it is clear that near the bubble
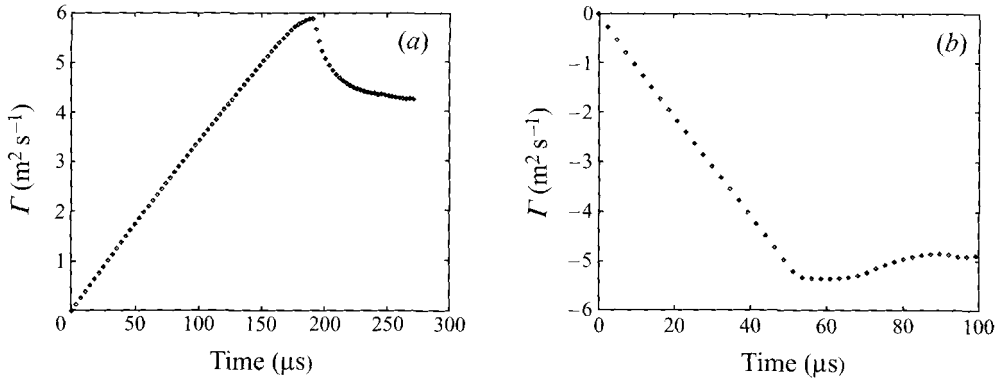
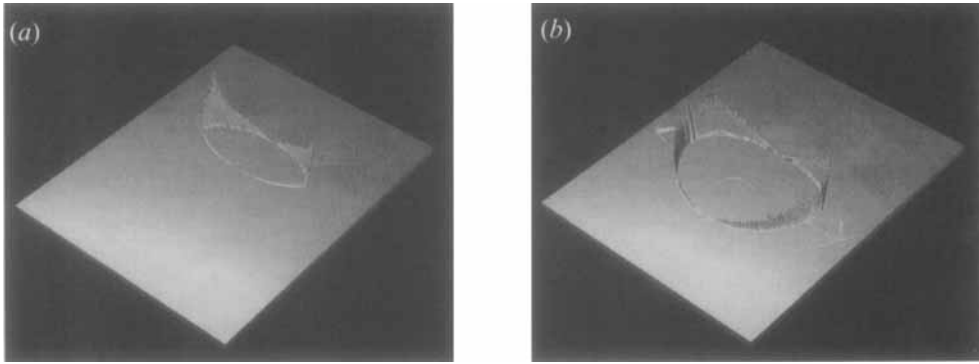FIGURE 15. Circulation as a function of time: (a) R22 bubble case; (b) He bubble case.

FIGURE 16. Surface plots of the magnitude of the vorticity field for the interaction of an $M_s = 1.22$ shock wave with an He cylindrical bubble. Times: (a) 32 μs, (e) 102 μs.

surface there are large deviations in the pressure gradient from the horizontal (see figure 10b, c).

Surface plots for the vorticity field and the baroclinic torque term indicate that vorticity production is effectively restricted to just two sites and that the amount produced by plain shock curvature is negligible (see figure 16). The bulk of the vorticity is produced where the side shocks interact with the bubble interface, point a on figure 11, hence the reason why the circulation bottoms out once the refracted shock emerges from the bubble. The other site is where the Mach stem crosses the bubble interface, point b on figure 11. But this site is only active during the windward part of the interaction. Both sites of vorticity production are extremely localized and cover only three or four mesh cells, i.e. a region just 0.2 mm in diameter. Because of this, they show up poorly on a graphic and no worthwhile plots can be presented. Interestingly, Picone & Boris (1988) did note that the production of vorticity along the bubble interface appeared to track the fastest moving shock wave, i.e. the side shock. However, the low resolution of their computations did not allow them to conclude this with any certainty and the error for the duration of vorticity production in the PB circulation model went unnoticed.

In the R22 bubble case it becomes even clearer that the pressure gradient which produces baroclinic torque does not remain horizontal. In fact, it generally acts in a direction tangential to the bubble interface, see figure 8(b–d). This observation is built into the SZ model and leads it to predict to first order that $\pi/2$ more circulation
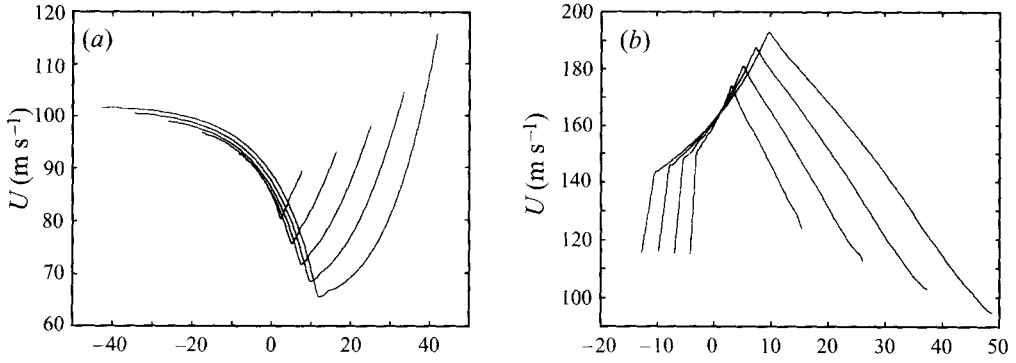
FIGURE 17. (*a*) Velocity distribution along the R22 bubble axis at times: (i) 33 μs, (ii) 68 μs, (iii) 101 μs, (iv) 133 μs, (v) 165 μs. (*b*) Velocity distribution along the He bubble axis at times: (i) 16 μs, (ii) 28 μs, (iii) 40 μs, (iv) 52 μs.

is produced over the leeward part of the interaction than over the windward part. This prediction, however, ignores the weakening of the incident shock jump, as it diffracts around the bubble (see figure 8*a–c*), which reduces its ability to produce vorticity. Our simulations indicate that the circulation actually increases uniformly up to $t = 180$ μs (see figure 15*a*) which is around the time when the refracted wave is focused to a point (see figure 7*d*). Now for this to happen, vorticity production over the leeward side of the bubble cannot be confined to a single point, and plots of the baroclinic torque term confirm that vorticity is generated along the interface over the extent of the washed out pressure gradient (again these plots are not presented, since the region of baroclinic activity merely forms an arc of the interface, one or two mesh cells thick, that runs backwards from where the shock intersects the bubble). Therefore models which only consider the shock front dynamics cannot be expected to produce reliable predictions for this phase of the vorticity deposition. Besides, the SZ model, which is based on an expansion for the exact vorticity production under the assumption of regular reflection, is probably too far outside its range of validity to provide an accurate prediction for this phase of the interaction.

In light of the present simulations we would argue that the accuracy of the PB, YKZ and SZ models rests with the insensitivity of circulation to the precise details of the vorticity deposition. Note that at any instant during the interaction, the circulation could be computed directly by performing the velocity contour integral

$$\oint_{ABCD} \boldsymbol{u} \cdot \mathbf{d}l$$

for the path ABCD shown in figure 6. Therefore provided no spurious reflections have taken place, there will be no contribution to the integral from the sides AB and CD, while that along BC simply comes from the constant velocity state behind the incident shock and so grows linearly with time. In fact, the only interesting contribution comes from a segment A′D′ which lies between the reflected and refracted shocks along the axis AD. Figure 17 shows snapshots of the velocity distribution along this segment during various stages of the two interactions studied here. Given the intricacies of the flows, it is somewhat surprising that the average velocity along the segment A′D′ remains almost constant in time (the average in the He bubble case is 151.6 m s^{-1} $\pm 1.4\%$ and that in the R22 case is 86.5 m s^{-1} $\pm 2.8\%$), thereby revealing

why the circulation increases uniformly with time in both interactions, at least up to the point where secondary effects come in to play.

9. Conclusions

Detailed numerical simulations have been performed in an attempt to shed new light on the complex phenomenological behaviour of shock waves interacting with gas inhomogeneities. The conditions of the simulations were chosen to match the experiments of Haas & Sturtevant (1987): a weak shock wave in air ($M_S = 1.22$) interacts with an isolated cylindrical bubble of either Refrigerant 22 or helium. In both cases the simulations reproduce the principal features observed in the experiments and even go so far as to expose certain features which were barely visible in the experimental shadowgraphs. The extent of the agreement lends credibility to several observations that are made using information gleaned from the simulations for which there is no experimental counterpart.

In particular, since the simulations provide full information for wave strengths and not just wave geometries, the precise nature of the refracted shock within the bubble inhomogeneities has been revealed for the first time. In the R22 bubble case it is shown that there are large variations in wave strength along the length of the refracted front; the two side limbs are very much weaker than the central portion, being little more than weak compressive systems that are not discontinuous but have a finite width. This behaviour accounts for the 'shock thickening' observed in the experiment, although optical distortions in the shadowgraph system appear to have exaggerated the effect.

Additionally, since computations do not suffer from repeatability problems and allow measurements that are non-intrusive, the simulations have allowed two weaknesses of the experiments to be quantified: the intrusive technique used to measure pressure gave readings that were between 37 and 51% too high; experimental scatter masked accelerations and decelerations of the flow features, e.g. the velocity for the upstream interface of the R22 bubble was measured as 73 m s^{-1}, missing a deceleration from 84 m s^{-1} to 61 m s^{-1}.

The present results also provide new insight into the process whereby baroclinic torque generates vorticity. In the helium bubble case it is found that it is the side shocks, where they cross the bubble interface, that are responsible for generating vorticity. Thus production effectively ceases once the refracted wave emerges from the bubble, even though the incident wave has traversed only half of the bubble by the time this happens. On the other hand, in the R22 bubble case it is found that vorticity production is not confined to a point over the leeward half of the interaction, because there is a continuous pressure gradient at the bubble interface, rather than a shock jump, owing to the diffraction of the incident wave. These observations undermine assumptions upon which current circulation prediction models are based, and would seem to suggest that it is insufficient to consider just the front dynamics when devising such models.

We point out, however, that at any instant during a shock–bubble interaction the only non-trivial contribution to the circulation rests with the velocity distribution along the bubble axis between the reflected and refracted waves. For the cases studied here, although this velocity distribution is both highly non-uniform and unsteady, it provides an averaged velocity that hardly varies over the course of the interaction (86.5 m s^{-1} $\pm$ 2.8% in the R22 bubble case, and 151.6 m s^{-1} $\pm$ 1.4% in the helium bubble case). Consequently circulation grows linearly with time and is independent

of the details of the flow. Moreover, these averaged velocities are within 3% of the interface velocity found by solving the appropriate one-dimensional Riemann problem for the instant the shock strikes the bubble, and this explains why under-resolved computations which completely miss the dynamics of the interaction still provide reasonable predictions for circulation. Similarly, we believe that the apparent success of current circulation prediction models rests on this insensitivity of the bubble-axis velocity to the precise details of the interaction.

REFERENCES

ABD-EL-FATTAH, A. M. & HENDERSON, L. F. 1978*a* Shock waves at a fast slow gas interface. *J. Fluid Mech.* **86**, 15–32.

ABD-EL-FATTAH, A. M. & HENDERSON, L. F. 1978*b* Shock waves at a slow fast gas interface. *J. Fluid Mech.* **89**, 79–95.

ABGRALL, R. 1988 Generalisation of the Roe scheme for the computation of mixture of perfect gases. *La Recherche Aérospatiale* **6**, 31–43.

BELL, J., BERGER, M., SALTZMAN, J. & WELCOME, M. 1994 Three-dimensional adaptive mesh refinement for hyperbolic conservation laws. *SIAM J. Sci. Comput.* **15**, 127–138.

BEN-DOR, G. & TAKAYAMA, K. 1985 Analytical prediction of the transition from Mach to regular reflection over cylindrical concave wedges. *J. Fluid Mech.* **158**, 365–380.

BERGER, M. J. & COLELLA, P. 1989 Local adaptive mesh refinement for shock hydrodynamics. *J. Comput. Phys.* **82**, 67–84.

BERGER, M. J. & OLIGER, J. 1984 Adaptive mesh refinement for hyperbolic partial differential equations. *J. Comput. Phys.* **53**, 482–512.

CATHERASOO, C. J. & STURTEVANT, B. 1983 Shock dynamics in nonuniform media. *J. Fluid Mech.* **127**, 539–561.

COLELLA, P., GLAZ, H. M. & FERGUSON, R. E. 1989 Multifluid algorithm for Eulerian finite difference methods. Manuscript (unpublished).

DRUMMOND, J. P. & GIVI, P. 1994 Suppression and enhancement of mixing in high-speed reacting flow fields. In *Combustion in High Speed Flows* (ed. J. Buckmaster, T. L. Jackson & A. Kumar), pp. 191–229. Kluwer.

GLIMM, J. & MCBRYAN, O. 1985 A computational Model for interfaces. *Adv. Appl. Maths* **6**, 422–435.

GRAHAM, R. L. 1969 Bounds on certain multiprocessing anomalies. *SIAM J. Appl. Maths* **17**, 416–429.

GROVE, J. W. & MENIKOFF, R. 1990 Anomalous reflection of a shock wave at a fluid interface. *J. Fluid Mech.* **219**, 313–336.

HAAS, J.-F. & STURTEVANT, B. 1987 Interaction of weak shock waves with cylindrical and spherical gas inhomogeneities. *J. Fluid Mech.* **181**, 41–76.

HENDERSON, L. F., COLELLA, P. & PUCKETT, E. G. 1991 On the refraction of shock waves at a slow-fast gas interface. *J. Fluid Mech.* **224**, 1–27.

HILLIER, R. 1991 Computation of shock wave diffraction at a ninety degrees convex edge. *Shock Waves* **1**, 89–98.

HOU, T. Y. & LE FLOCH, PH. 1994 Why nonconservative schemes converge to wrong solutions: Error analysis. *Math. Comput.* **62**, 497–530.

KARNI, S. 1992 Viscous shock profiles and primitive formulations. *SIAM J. Numer. Anal.* **29**, 1592–1609.

KARNI, S. 1994 Multi-component flow calculations by a consistent primitive algorithm. *J. Comput. Phys.* **112**, 31–43.

KARNI, S. 1995 A level-set capturing scheme for compressible interfaces. In *Numerical Methods for Wave Propagation Phenomena* (ed. E. F. Toro). Kluwer.

LARROUTUROU, B. 1991 How to preserve the mass fractions positive when computing compressible multi-component flows. *J. Comput. Phys.* **95**, 59–84.

LAX, P. D. 1954 Weak solutions of nonlinear hyperbolic equations and their numerical computation. *Commum. Pure Appl. Maths* **7**, 159–163.

LAX, P. D. 1972 *Hyperbolic Systems of Conservation Laws and the Mathematical Theory of Shock Waves.* SIAM Monograph Series.

LÖHNER, R., PICONE, J. M. & BORIS, J. P. 1988 Wave structure produced by shock propagation through a dense bubble gas. In *Proc. 16th Intl Symp. on Shock Tubes and Waves, Aachen, Germany 1987, Weinheim, Germany, 1988.* (ed. by H. Gronig), pp. 613–619. VCH, Weinheim.

MARBLE, F. E., HENDRICKS, G. J. & ZUKOSKI, E. E. 1987 Progress toward shock enhancement of supersonic combustion processes. *AIAA Paper* 87-1880.

MESHKOV, Y. Y. 1970 Instability of a shock wave accelerated interface between two gases. *NASA Transl.* TT F-13, 074 R.F.

NEUMANN, J. VON 1963 *Collected Works*, vol. 6. Pergamon Press.

PICONE, J. M. & BORIS, J. P. 1988 Vorticity generation by shock propagation through bubbles in a gas. *J. Fluid Mech.* **189**, 23–51.

PUCKETT, E. G. & SALTZMAN, J. S. 1992 A 3-D adaptive mesh refinement algorithm for multi-material gas dynamics. *Physica D* **60**, 84–104.

QUIRK, J. J. 1991 An adaptive mesh refinement algorithm for computational shock hydrodynamics. PhD Thesis, Cranfield Institute of Technology, UK.

QUIRK, J. J. 1994 A contribution to the great Riemann solver debate. *Intl J. Numer. Meth. Fluids* **18**, 555–574.

QUIRK, J. J. 1996 A parallel adaptive mesh refinement algorithm for computational shock hydrodynamics. To appear in *Appl. Numer. Maths.*

RICHTMYER, R. D. 1960 Taylor instability in shock acceleration of compressible fluids. *Commun. Pure Appl. Maths* **23**, 297–319.

ROE, P. L. 1982 Fluctuations and signals - A framework for numerical evolution problems. In *Numerical Methods for Fluid Dynamics* (ed. K. W. Morton & M. J. Baines), pp. 219–257. Academic.

RUPERT, V. 1992 Shock-interface interaction: current research on the Richtmyer-Meshkov problem. In *Shock Waves, Proc. 18th Intl. Symp. on Shock Waves, Sendai, Japan 1991* (ed. K. Takayama), pp. 83–94. Springer.

SAMTANEY, R. & ZABUSKY, N. J. 1994 Circulation deposition on shock-accelerated planar and curved density-stratified interfaces: models and scaling laws. *J. Fluid Mech.* **269**, 45–78.

SCHWENDEMAN, D. W. 1988 Numerical shock propagation in non-uniform media. *J. Fluid Mech.* **188**, 383–410.

SHERCLIFF, J. A. 1977 *Vector Fields*, p. 276. Cambridge University Press.

STRANG, G. 1968 On the construction and comparison of finite-difference schemes. *SIAM J. Numer. Anal.* **5**, 506–517.

TON, V. T., KARAGOZIAN, A. R., ENGQUIST, B. E. & OSHER, S. J. 1991. Numerical simulation of inviscid detonation waves with finite rate chemistry. *Proc. Combustion Inst. 1991 Fall Meeting, UCLA, Paper* WSS/C91-101, pp. 482–512.

VAN DYKE, M. 1982 *An Album of Fluid Motion* p. 148, The Parabolic Press, Stanford, California.

WANG, J. C. T. & WIDHOPF, G. F. 1990 Numerical simulation of blast flowfields using a high resolution TVD finite volume scheme. *Computers & Fluids* **18**, 103–137.

WHITHAM, G. B. 1957 A new approach to problems of shock dynamics. Part 1. Two dimensional problems. *J. Fluid Mech.* **2**, 145–171.

WHITHAM, G. B. 1958 On the propagation of shock waves through regions of non-uniform area or flow. *J. Fluid Mech.* **4** 337–360.

YANG, J., KUBOTA, T. & ZUKOSKI, E. E. 1993 Applications of shock-induced mixing to supersonic combustion. *AIAA J.* **31**, 854–862.

YANG, J., KUBOTA, T. & ZUKOSKI, E. E. 1994 A model for characterization of a vortex pair formed by shock passage over a light-gas inhomogeneity. *J. Fluid Mech.* **258**, 217–244.

ZWAS, G. & ROSEMAN, J. 1973 The effect of nonlinear transformations on the computation of weak solutions. *J. Comput. Phys.* **12**, 179–186.